An Adaptive, Statistical Multiscale Phase Unwrapping Approach to Process Large Swath Interferograms

Pietro Mastro, Antonio Pepe, *Senior Member*, *IEEE*, and Cathleen E. Jones, *Member*, *IEEE*

***Abstract*— This study investigates the potential of a statistical-based, adaptive approach to unwrapping sequences of differential synthetic aperture radar (SAR) interferograms that cover a large swath of the terrain. The proposed method adopts a multiscale decomposition strategy to identify efficiently and then process sets of coherent points at different spatial scales. The coherent point selection process is performed considering the statistical properties of the stack of wrapped multilooked SAR interferograms generated at various scales. Overall, the adopted procedure allows automatically recognizing the areas in large swath interferograms where significant and reliable phase changes occur while moving from neighboring spatial scales. Over these regions, multiscale phase unwrapping (PhU) operations are performed efficiently, with a computational improvement and without losing significant information. To this aim, the implementation of a conditioned space-time PhU scheme that operates sequentially at different spatial grids is detailed. Then, the unwrapped interferograms are inverted to generate ground displacement time series through advanced multitemporal interferometric SAR (MT-InSAR) approaches, recovering information at different scales (from local to regional/continental). Experimental results have been obtained by applying the developed scheme to large-swath SAR datasets collected at the C band by Sentinel-1 sensors. The results demonstrate the feasibility and soundness of the developed multiscale PhU method.**

***Index Terms*— Circular statistics, ground deformations, interferometric synthetic aperture radar (InSAR), multiscale, phase unwrapping (PhU).**

I. INTRODUCTION

DIFFERENTIAL synthetic aperture radar interferometry (DInSAR) [1], [2] presently is a consolidated and reliable technique that is routinely applied for detecting and studying ground surface displacements and monitoring their temporal modifications. DInSAR has gained increasing consideration over the last three decades due to its ability to measure ground surface displacements with a dense grid of measurement points, which is the essential distinguishing feature of the DInSAR technology with respect to other conventional approaches (e.g., GPS and leveling measurement campaigns). This technology has primarily been adopted to study and analyze distinctive Earth's surface displacements caused by natural (e.g., volcanic eruptions [3], [4], earthquakes [5], [6], coastal erosion phenomena, and sea-level-rise effects [7]) or anthropic (e.g., over-pumping groundwater and geothermal fluids [2], underground mining [8], and land reclamations procedures [9]) sources. Notably, for anthropogenic sources, DInSAR provides information used to identify, respond to, and help prevent the inevitable harmful consequences caused by severe ground displacement (subsidence) phenomena, which can structurally damage buildings, railways, highways, dikes, and underground lifeline pipelines.

Several multitemporal differential synthetic aperture radar (SAR) interferometry methods have been developed to investigate ground displacement signals related to pointwise [10] and distributed targets [11], [12], [13] on the terrain. Irrespective of their unique characteristics, the different existing methods have in common the primary need to identify a reliable set of coherent points over which the subsequent phase unwrapping (PhU) operations are performed. Historically, efficient PhU methods, which operate on single interferograms by considering only spatial constraints, were developed (e.g., [14], [15], [16], [17], [18], [19], [20], [21]). Subsequently, the temporal information among sets of multitemporal SAR interferograms was exploited by 3-D and hybrid space/time novel PhU algorithms (e.g., [22], [23], [24], [25]) or error-correcting algorithms [26], [27].

Present-day and future SAR missions [28], [29] are increasingly making possible the acquisition of SAR images with enhanced spatial resolutions, extensive spatial coverage, and short revisiting times. In this context, the generation of long-term ground deformation time series with dense spatial grids of the measurements is becoming problematic from the computational point of view, especially over regions where the density of coherent points is very high or when the investigated area is large.

To deal with the processing of large SAR datasets, divide-and-merging PhU operations [30], [31], [32], [33] are typically

---

Received 30 May 2024; revised 17 September 2024; accepted 3 November 2024. Date of publication 7 November 2024; date of current version 9 December 2024. This work was supported in part by the Jet Propulsion Laboratory (JPL), California Institute of Technology, Pasadena, CA, USA, through the Short-Term Mobility (STM) Program of the National Research Council of Italy in 2023 and through the National Aeronautics and Space Administration under Contract 80NM0018D0004; in part by the European Space Agency (ESA) under the ESA GREENISH Tender; in part by the National Recovery and Resilience Plan (NRRP), Mission 4, Component 2, Investment 1.1, Program PRIN 2022, through "Multiscale Study of Seismogenic Processes in Campania-Lucania Apennines Using Machine Learning Algorithms and Multiparametric Observations (FRACTURES)" Project; and in part by the European Union-Next Generation EU, CUP B53D23006980006 under Grant 2022BEKFN2. *(Corresponding author: Pietro Mastro.)*

Pietro Mastro and Antonio Pepe are with the Istituto per il Rilevamento Elettromagnetico dell'Ambiente, Italian National Research Council, 80125 Naples, Italy (e-mail: mastro.p@irea.cnr.it; pepe.a@irea.cnr.it).

Cathleen E. Jones is with the Jet Propulsion Laboratory, California Institute of Technology, Pasadena, CA 91125 USA (e-mail: cathleen.e.jones@jpl.nasa.gov).

Digital Object Identifier 10.1109/TGRS.2024.3493596

carried out. They generally consist of 1) splitting the dataset into small tiles that are; 2) then independently unwrapped; and 3) finally mosaicked to ensure the continuity of the solutions over the overlapped regions. To obtain reliable unwrapped results over disconnected and/or incoherent regions, region-growing methods [15], [19], [34] and constrained network optimization procedures [12], [35], [36] have also been implemented. Furthermore, more recently, deep learning and compressed sensed [34], [37], [38] methods have been used to solve the twofold problem of automatically identifying regions with significant deformation signals and unwrapping them efficiently.

In this study, we present an adaptive, statistical-based segmentation method for the processing of large swath SAR datasets that relies on a quad-tree decomposition strategy [39] and yields DInSAR deformation products (e.g., mean displacement velocity maps and relevant time series) at different resolution scales [19]. The developed method permits adaptively changing (i.e., increase/decrease) the density of the spatial grids at various resolution scales to identify those regions where significant phase changes occur upon moving from one resolution scale to another. The method also automatically adjusts the spatial grids of PhU operations to circumvent problems due to incorrect sampling of the wrapped phase data at different scales. The developed method is tested on real SAR datasets, and its implications for the efficient processing of stacks composed of many large-swath multitemporal SAR interferograms are explored.

This article is organized as follows. Section II summarizes the basic rationale of constrained network PhU optimization with its implications for processing large swath SAR interferograms. Section III presents an adaptive, statistical-based segmentation method for large SAR datasets to reliably identify regions at different resolution scales on which to perform the subsequent PhU operations detailed in Section IV. Experimental results for real SAR datasets in the U.S. and Italy are shown in Section V. Algorithms performances are derived in Section VI, and the conclusion is presented in Section VI.

II. FUNDAMENTALS OF LARGE SWATH PHU

Section II-A first introduces the theoretical framework of the problem of unwrapping large swath interferograms using multigrid approaches. Then, Section II-B summarizes the general formulation of the constrained network PhU problem, which is at the core of the implemented PhU scheme presented in Sections III and IV.

A. Multigrid PhU of Large Datasets

PhU [14], [40], [41] constitutes a critical processing step employed by technologies such as SAR interferometry [42] to estimate the phase history of recorded signals. If we consider a (wrapped) interferogram, namely, ϕ, the solution of a PhU problem generally involves searching for the (unknown) 2π-integer multiples that must be added to the measured (wrapped) phases to get the unwrapped (full) interferometric phases, ψ. Accordingly

$$\psi(P) = \phi(P) + 2\pi K(P) \tag{1}$$

where P refers to a generic point of the 2-D (spatial) discrete grid V of coherent pixels of the azimuth/range domain.

Over the years, numerous PhU algorithms have been proposed (e.g., [17], [18], [20], [41]) to address the inherent challenges in the processing of interferometric SAR (InSAR) data, initially by exploiting exclusively spatial information and independently unwrapping single interferograms. Recently, the interest has progressively moved toward the development of PhU methods that can incorporate spatial and temporal constraints (3-D) [22], [23], [24], [25], [43] as well as those that exploit machine-/deep-learning approaches [34], [36], [37], [38], [44].

The improved resolutions (spatial and temporal) and spatial coverage of SAR images collected by current and upcoming SAR missions [28], [45], [46] have brought about new challenges related to the need to generate and process long-term sequences of SAR interferograms covering large areas of terrain and recover spatially dense maps of ground displacements [4], [10], [11], [47].

In this context, a relevant concern arises from the dimensions of the interferometric input datasets, which often surpass the limits imposed by hardware constraints or throughput requirements. The most straightforward PhU solutions in the literature consist of splitting the problem of unwrapping large-swath interferograms as a mosaic of PhU solutions attained on smaller blocks [30], [31], [48], [49]. Generally, these methods partition an InSAR dataset (i.e., an interferogram) into a series of small blocks, process each block independently, and then integrate the resulting blocks into the result. However, despite the significant reduction in processing time achieved by these algorithms, the block-division approach poses challenges in the PhU operation [30], [31], [49]. This is primarily due to the difficulty of obtaining a global solution based solely on the local solutions of the processed blocks.

In this framework, the use of multigrid approaches has offered a different practical solution to the 2-D (spatial) PhU [19], [50], [51], [52]. They consist of discretizing the operation over a set of grid points of the spatial domain and solving a system of algebraic equations linked to the chosen grid points with specific boundary conditions.

Examples of multigrid PhU methods can be found in the literature [28], [62]. An L_1 oriented multigrid method, in particular, was initially proposed in [51]. The algorithm adopts a tile PhU approach [30], with a recursive quad-tree-like strategy to overcome tile PhU problems by identifying homogeneous regions utilizing a bottom-up approach, leveraging the homogeneity of individual pixels. For instance, a 2 × 2 homogeneous area is constructed by examining the phase values at the interfaces between the four adjacent regions, with larger areas scaled up accordingly. The recursion terminates upon detecting a homogeneous area. Subsequently, tiles at the same level are recombined by minimizing the L_1 norm PhU error at the interfaces between adjacent regions. The recombination step facilitates avoidance of low-modulation/highly noisy areas by employing a phase-weighting matrix to nullify their contribution to the PhU error (see [51, eqs. (3) and (5)]), enhancing the unwrapping process. In addition, interface error checking inherently limits the probability of error propagation.

Multigrid PhU problems that solve least-squares (LSs) optimization problems, which rely on minimizing the discrete partial differential equations (PDEs) between the wrapped and unwrapped phase data, have been developed [27], [45], [65]. In this case, the multigrid PhU problem involves transferring the PhU operation to coarser grids, applying the Gauss-Seidel relaxation scheme [55], [56], [57], [58], and then transferring the intermediate solutions back to the finer grids. The full multigrid (FMG) approach proposed by Lisano et al. [28] belongs to this class. The algorithm's core concept involves storing phase partial derivatives in separate arrays and correcting them at the coarser grid boundaries using an L_2 norm minimization. A notable feature of the FMG method is that the lower sampling rates of the phase signal on coarser grids magnify the spatial frequencies of the residual error, facilitating the transfer of low-frequency information from finer to coarser grids. As a result, global solutions at finer levels contribute to local solutions at coarser levels, thus simplifying the solving process and enhancing the overall effectiveness of the Gauss-Seidel relaxation scheme. Overall, numerical experiments have shown that multigrid PhU algorithms are fast and robust, especially in areas with medium to high signal-to-noise ratios (SNRs) [19], [51].

B. Rationale of Constrained PhU Operations

The developed multiscale PhU scheme, detailed in Sections III and IV, implements a series of constrained network optimization problems. In this section, we concisely summarize the fundamental rationale of the (weighted) minimum L_p norm-constrained PhU problem [52], [54], which was initially presented in [35] and adapted in [12], [59], [60], and [61] to solve spatial and temporal PhU problems.

A constrained PhU problem allows computation of unwrapped phases, $\psi(P), \forall P \in V$, over a discrete sparse grid of points, v, subject to the additional constraint that the unwrapped phases related to a subset of coherent radar pixels, $V' \subseteq V$, are a priori known, namely, $\psi(Q) = \psi'(Q) \forall Q \in V'$, where ψ' is the field of previously recovered (known) unwrapped phases. To solve this problem, a "primary" planar-connected graph, $G' = \{V', E'\}$, is first constructed from the set of constrained (bounded) points of the azimuth/range spatial domain, V', where E' is the set of edges (connecting arcs) of the planar graph, G', which, for instance, can be obtained by computing a (Delaunay) triangulation in the azimuth/range domain. Subsequently, we consider a "secondary" connected constrained planar graph, $G = \{V, E\}$, that involves all coherent radar pixels, V, and contains all the edges of the primary grid (i.e., $E \supseteq E'$). This secondary graph can be retrieved using a constrained Delaunay triangulation (CDT) [12], [35].

An example of a CDT is sketched in Fig. 1. In particular, Fig. 1(a) shows the discrete set of points (blue) over which the constrained arcs of a CDT (black lines) are identified. Fig. 1(b) shows a zoomed-in view of the generated CDT related to the constrained arcs of the "primary" triangulation that are highlighted in red in Fig. 1(a).

The constrained L_p optimization problem to be solved is the following:

$$\psi = \text{argmin}\left[\sum_{q=1}^{N_E} w_q |\Delta\psi_q - \Delta\phi_q|^p\right] \tag{2a}$$

$$\text{subject to}\, \psi(P) = \psi'(P) \quad \forall P \in V' \tag{2b}$$

where $\Delta\psi_q = \psi(A_q) - \psi(B_q)$ and $\Delta\phi_q = \langle\phi(A_q) - \phi(B_q)\rangle_{-\pi,\pi}$ are the set of unwrapped and wrapped phase gradients computed over the selected qth edge of the graph $G = \{V, E\}$, respectively; $\langle\cdot\rangle_{-\pi,\pi}$ is the wrapping operation and $e_q = (A_q, B_q)$ are the vertices of the generic q th edge; N_E is the number of edges and w_q are the weights associated with the graph edges. It has already been shown that the problem in (2) is equivalent to the following [12], [35]:

$$\psi = \text{argmin}\left[\sum_{q=1}^{N_E} \mu_q |\Delta\psi_q - \Delta\zeta_q|^p\right] \tag{3a}$$

with

$$\mu_q = \begin{cases} w_q, & e_q \notin E' \\ L, & e_q \in E', \end{cases} \qquad \Delta\zeta_q = \begin{cases} \Delta\phi_q, & e_q \notin E' \\ \Delta\psi'_q, & e_q \in E' \end{cases} \tag{3b}$$

where w_q is the weight of the q th edge of the computed CDT, L is a large number (representing the infinite value), and $\Delta\zeta_q$ includes the known unwrapped phase gradients over the constrained edges, $E' \subseteq E$, of the secondary graph $G = \{V, E\}$.

Note that the problem in (3) with $p = 1$ can be solved with minimum cost flow (MCF) networks [62], [63], [64] using efficient network programming codes, as with the RELAX IV solver [65].

A few additional remarks on the solution of the constrained PhU problem in (3a) and (3b) are now in order. For the sake of ease, let us consider again the primary and secondary graphs of the example shown in Fig. 1. It is worth noting that while solving the MCF problem corresponding to the secondary graph, the phase residuals (i.e., the curl of the phase gradients calculated over every closed triangular loop) for every triangle of the computed CDT must be evaluated. Considering the generic triangle of the CDT, whose arcs are labeled α, β, and γ, the phase residuals are computed as follows: $r_{\alpha\beta\gamma} = \Delta\zeta_\alpha + \Delta\zeta_\beta + \Delta\zeta_\gamma$. However, since the costs of the constrained arcs [i.e., those labeled in red in Fig. 1(b)] are large and the phase gradients of the constrained ares are computed from a set of a priori known unwrapped phases [see the constraints (3b)], the following critical conditions are verified.

1) The net phase residuals inside any convex envelope of the primary graph (e.g., the hth triangle Tr_h of the primary graph) is equal to zero, namely, $\sum_{\text{Tr}_h} r_{\alpha\beta\gamma} = 0$.

2) While the relevant MCF network problem (3a) and (3b) is solved, the equivalent fluxes that are generated to compensate for the negative and positive residuals into these triangular-shaped envelopes remain confined to these regions.

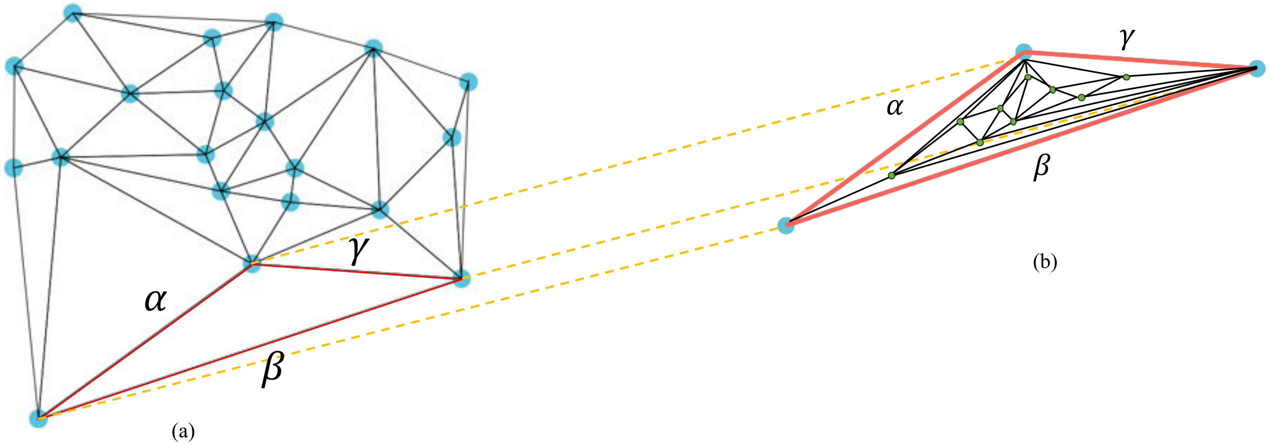

Fig. 1. Example of a CDT. (a) Constrained arcs and (b) triangle of the CDT [red in (a)] at the next finer resolution scale, relevant to a set of points portrayed in green.

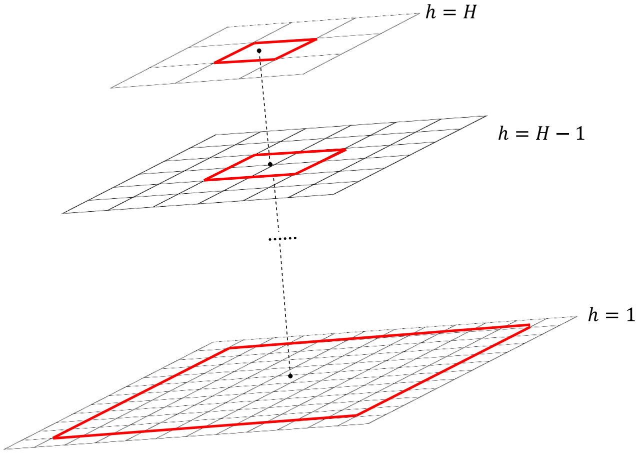

Fig. 2. Multiscale resolution scheme. The resolution decreases by half in each layer from finest ($h = 1$) to coarsest ($h = H$).

Accordingly, there is no possibility that additional corrections of the unwrapped phase gradients over the bounded arcs of the CDT could be found (indeed, any equivalent flux that crosses a bounded arc would be associated with a large cost value).

3) Any triangular (convex) envelope of the primary graph can be seen as a separate tile that could ideally be processed independently. As a consequence, the final unwrapped solutions computed on the whole set of point, V, has no phase discontinuities, as happens for the constrained PhU global solution. As detailed in Section IV, the latter property is paramount for unwrapping large swath interferograms.

III. ADAPTIVE, STATISTICAL-BASED MULTISCALE SEGMENTATION APPROACH

To describe the method proposed for the unwrapping of large swath interferograms and the subsequent generation of multiscale ground deformation products, let us consider a group of N SAR images collected at the ordered times, collected at the ordered times, $t = [t_0, t_1, \ldots, t_{N-1}]$, which are preliminarily co-registered to a common reference image. Starting from this dataset, a series of M InSAR data pairs are selected. Let $[\Delta t_1, \Delta t_2, \ldots, \Delta t_M]$ and $[\Delta b_{\perp 1}, \Delta b_{\perp 2}, \ldots, \Delta b_{\perp M}]$ be the vectors of the temporal and perpendicular baseline associated with the selected InSAR data pairs.

The adopted multiscale PhU approach requires generating some sequences of M multilooked differential SAR interferograms at H distinctive resolution scales. Specifically, let

$$\mathbf{\Phi}^{(h)} = \left[\phi_0^{(h)}, \phi_1^{(h)}, \ldots, \phi_{M-1}^{(h)}\right] \quad h = 1, 2, \ldots, H \tag{4a}$$

and

$$\mathbf{\Psi}^{(h)} = \left[\psi_0^{(h)}, \psi_1^{(h)}, \ldots, \psi_{M-1}^{(h)}\right] \quad h = 1, 2, \ldots, H \tag{4b}$$

be the (known) wrapped and (unknown) unwrapped multilooked SAR interferograms at the considered resolution scales, respectively, where ${N_{\mathrm{az}}}^{(h)}$ and ${N_{\mathrm{rg}}}^{(h)}$ are the azimuth and range multilook factors adopted for the hth generic scale. For the sake of simplicity, we also assume that the azimuth (range) looks double moving from adjacent scales: ${N_{\mathrm{az}}}^{(h)} = 2{N_{\mathrm{az}}}^{(h-1)}({N_{\mathrm{rg}}}^{(h)} = 2{N_{\mathrm{rg}}}^{(h-1)})$, and the $h = 1$ grid has the finest spatial spacing (see Fig. 1). It is worth remarking that the latter grid does not necessarily correspond with the single-look scale. We also assume that PhU operations can be straightforwardly carried out at the $h = H$ scale, with no need to further reiterate the developed PhU procedure to coarser scales, the number of detectable coherent SAR pixels at that scale being less than a critical value (i.e., the maximum number of pixels that must be processed considering the temporal extent of the SAR datasets and the available hardware capabilities).

In this section, we preliminarily focus on the problem of identifying a reliable set of SAR pixels at the different resolution scales over which the proposed network-constrained multiscale PhU technique (see Section IV) is subsequently applied. To this aim, a statistical, multigrid segmentation algorithm is fully detailed. The algorithm exploits circular variance statistics [66]; it is implemented to identify, at the generic hth scale, a group of reliable, coherent SAR pixels, denoted as $\Omega^{(h)}$, over which the gradient of the (wrapped) phase signal from the $h + 1$th to the hth scale is appreciable. This way, the PhU procedure is implemented at the coarser resolution scales only on a reduced number of points, which

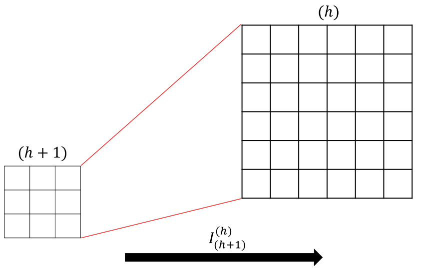

Fig. 3. Interpolation operation from the coarser grid $h + 1$th to the finer hth grid.

are, however, sufficient to retrieve and follow the spatial dynamic of the (global) "true" signals inherent to every single spatial scale.

The implemented procedure recursively moves from the coarsest ($h = H$) to the finest ($h = 1$) scale. Considering the generic hth scale, it consists of the following steps.

1) First, a set of coherent SAR pixels is determined at the hth scale by exploiting the phase triangulation property of multilooked SAR interferograms and calculating the triangular coherence factor as follows [35], [67]:

$$\gamma^{(h)} = \frac{1}{\mathrm{Tr}} \left| \sum_{k=1}^{\mathrm{Tr}} \exp\left[j\phi_{\mathrm{Tr},k}^{(h)} \right] \right| \in [0, 1] \tag{5}$$

where Tr is the number of triplets that can be computed considering the M interferograms generated at the generic scale h, $\phi_{\mathrm{Tr},k}^{(h)}$ is the curl of the wrapped multilooked phases over the kth triangle, and $j = \sqrt{-1}$ is the imaginary unit.

2) The second step concerns the estimation of the low-pass (LP) phase stack at the scale h based on the phase values at the $h + 1$ scale as follows:

$$\phi_{\mathrm{LP},k}^{(h)} = \arctan\left(\frac{I_{(h+1)}^{(h)}\left(\sin\left(\phi_k^{(h+1)}\right)\right)}{I_{(h+1)}^{(h)}\left(\cos\left(\phi_k^{(h+1)}\right)\right)} \right) k = 1, \ldots, M \tag{6}$$

where $I_{(h+1)}^{(h)}$ is the operator that interpolates the signal from the coarser $h + 1$th grid to the finer hth grid (see Fig. 3).

3) The third step concerns the determination of the following interscale high-pass (HP) phase components, which is mostly insensitive to atmospheric phase artifacts:

$$\phi_{\mathrm{HP},k}^{(h)} = \langle \phi_k^{(h)} - \phi_{\mathrm{LP},k}^{(h)} \rangle_{-\pi,\pi}, k = 1, \ldots, M. \tag{7}$$

4) The circular variance [66] of the HP phase components is thus computed

$$\mathrm{Var}^{(h)} = 1 - \frac{1}{M} \left| \sum_{k=0}^{M-1} e^{j\left(\phi_{\mathrm{HP}}^{(h)}\right)} \right|. \tag{8}$$

5) Finally, only SAR pixels characterized by a significant HP phase component, selected as those with a circular variance, $\mathrm{Var}^{(h)}$, exceeding a fixed threshold, t_1, and with a triangular coherence, $\gamma^{(h)}$, greater than a threshold, t_2, are selected to form the set of reliable, coherent SAR pixels, $\Omega^{(h)} = \{P : \mathrm{Var}^{(h)} \geq \mathrm{th}_1\} \cap \{P : \gamma^{(h)} \geq \mathrm{th}_2\}$, over which the subsequent PhU operations are performed (see Section IV for more details). To further reduce the number of SAR pixels to be processed at the hth scale, a quadtree segmentation process [51], [68], [69], [70] is also implemented. In this case, the set of reliable, coherent pixels characterized by significant HP phase residuals is iteratively computed as follows:

$$\Omega^{(h)} = \left\{ P : \mathrm{Var}^{(h)} \geq \mathrm{th}_1 \right\} \cap \left\{ P : \gamma^{(h)} \geq \mathrm{th}_2 \right\} \cap I_{(h+1)}^{(h)}\left(\Omega^{(h+1)}\right).$$

Concerning the coarser scale, i.e., with $h = H$, the coherent SAR pixels at this scale are straightforwardly selected using only the triangular coherence: $\Omega^{(H)} = \{P : \gamma^{(H)} \geq \mathrm{th}_2\}$ and the cardinality of this dataset is assumed less than the maximum number of points that must be processed considering the hardware capabilities constraints and the adopted thresholds.

Finally, at the finest grid, i.e., with $h = 1$, the set of coherent points is determined as $\Omega^{(1)} = \{P : \mathrm{Var}^{(1)} \geq \mathrm{th}_1\} \cap \{\mathbf{P} : \gamma^{(1)} \geq \mathrm{th}_2\} \cup \{P : \gamma^{(1)} \geq \mathrm{th}_3\}$ where $\{P : \gamma^{(1)} \geq \mathrm{th}_3\}$ is introduced to preserve the very coherent targets (with $\mathrm{th}_3 \gg \mathrm{th}_2$) that can be analyzed at the finest grid.[1]

IV. MULTISCALE PHU OF LARGE-SWATH SAR INTERFEROGRAMS

This section describes the main steps of an efficient PhU strategy for large swath datasets that combines multiscale global and local solutions in a unique framework, guaranteeing a good balance between computational burden and algorithm efficiency.

The final goal is to unwrap the interferograms at the finest scale, using the (global) unwrapped solutions obtained at the different spatial resolution scales. Indeed, at the finest resolution scale, the number of detected coherent pixels can exceed the maximum number of points that PhU solvers can simultaneously process, considering the spatial extent of the processed swaths, the hardware limitation, and the overall computation time. To circumvent these problems, a multiscale PhU scheme, which iteratively operates at different H scales, is proposed. The number of resolution scales, H, depends on the spatial extent of the imaged swaths (from local to regional/continental) as well as on the number of threats/cores that could be occupied once dynamic programming algorithms [71] are used to solve the PhU problem.

To this aim, a constrained PhU optimization (see Section II-B for details) is implemented at the generic hth scale.

A. Constrained Primary-Graph PhU

The primary graph of the constrained PhU procedure, $G'^{(h)} = \{\Omega'(h), E'(h)\}$, is built upon a set of very coherent points, $\Omega'(h)$, whose unwrapped phases are known, having been recovered from the (global) PhU solutions computed at the $h + 1$ higher scale, $\psi_i^{(h+1)}$. In particular, the unwrapped phases of the (bounded) constrained points, $\psi_i^{(h)}(\Omega'^{(h)})$, are obtained by first spatially interpolating the PhU solution, $\psi_i^{(h+1)}$, on the grid of coherent points at the hth scale $\Omega'(h)$, thus obtaining the signal $\widehat{\psi}_i^{(h)}(\mathbf{\Omega}'(h)) = I_{(h+1)}^{(h)}(\psi_i^{(h+1)})(\Omega'^{(h)})$, and then using the following mathematical relation:

$$\psi_i^{(h)}\left(\Omega'^{(h)}\right) = \widehat{\psi}_i^{(h)}\left(\Omega'^{(h)}\right) + \langle \phi_i^{(h)}\left(\Omega'^{(h)}\right) - \widehat{\psi}_i^{(h)}\left(\Omega'^{(h)}\right) \rangle_{-\pi,+\pi}$$
$$i = 1, \ldots, M. \tag{9}$$

---

[1] If the finest resolution grid corresponds to the single-look scale, the triangular coherence cannot be calculated, and it can be substituted, for instance, by the spectral diversity factor defined by Equation 2 of [67].

Equation (9) relates the unwrapped phase of the ith interferogram at the hth scale, $\psi_i^{(h)}(\Omega'(h))$, with the interpolated (global) unwrapped solution obtained at the higher $h+1$ scale $\widehat{\psi}_i^{(h)}(\Omega'(h))$, where the second terms on the right-hand side of (9) is mandatory to have unwrapped phases that differ from the wrapped ones by integer multiples of 2π.

The set of very coherent points for which the phase is well-constrained by PhU at higher scales, $\Omega'(h)$, is identified as follows. At the h th scale, the points $\Omega'^{(h)}$ do not belong to $\Omega^{(h)}$ and are selected among those very coherent, i.e., $\{P : \gamma^{(h)}(P) \geq \mathrm{th}_2\}$, for which the relevant HP phase residuals between the neighboring $h+1$ and h scales [see (7)] are minimal to reliably assume that they do not require further unwrapping. Similar to what was done in Section III, the circular variance of the HP phase residuals, $\mathrm{Var}^{(h)}$, is considered [see (8)]. However, in this case, the pixels to be selected are those with small values of the HP circular variance. A preliminary set of candidate SAR pixels over which to retrieve the (bounded) PhU values through (9) is selected based on a "first guess" at the circular variance threshold, $\varepsilon \ll \mathrm{th}_1$, applying the criteria

$$\Omega_\varepsilon^{(h)} \equiv \left\{P : \mathrm{Var}^{(h)}(P) \leq \varepsilon\right\} \cap \left\{P : \gamma^{(h)}(P) \geq \mathrm{th}_2\right\}. \tag{10}$$

The set is also refined by applying an additional test to verify the correctness of the unwrapped phases $\psi_i^{(h)}$ at the coherent candidate points location, $\Omega_\varepsilon^{(h)}$, computing their temporal coherence, ρ [see 34]. To this aim, the following LSs problem[2] is solved:

$$A \cdot \mathbf{\Phi}^{(\mathbf{h})} = \boldsymbol{\psi}^{(h)} \tag{11}$$

where $\mathbf{\Phi}^{(\mathbf{h})}$ is the phase vector associated with the SAR acquisitions. Then, starting from $\mathbf{\Phi}^{(\mathbf{h})}$, the vector of phase residuals

$$\boldsymbol{r}^{(h)} = \boldsymbol{A} \cdot \boldsymbol{\Phi}^{(h)} - \boldsymbol{\psi}^{(\mathbf{h})} \tag{12}$$

is computed. Hence, the temporal coherence factor ρ is finally calculated as follows:

$$\rho = \frac{\left|\sum_{k=0}^{M-1} e^{j r_k^{(h)}}\right|}{M}. \tag{13}$$

Only those pixels belonging to $\boldsymbol{\Omega}_\varepsilon^{(h)}$ that are characterized by very high values of the temporal coherence (e.g., higher than 0.9) are selected as the bounded points for the constrained PhU optimizations performed at the h th scale, i.e.,

$$\Omega'^{(h)} \equiv \Omega_\varepsilon^{(h)} \bigcap \left\{P : \rho^{(h)}(P) \geq 0.9\right\}. \tag{14}$$

B. Constrained Secondary-Graph PhU

The secondary graph, $G^{(h)} = \{\Omega^{(h)}, E^{(h)}\}$, refers to a set of coherent points, $\Omega^{(h)}$, identified at the given h scale (see Section III) for which the phase solution must be refined, i.e., those with large values of the HP circular variance. Over these points, the (local) PhU solutions are computed by solving constrained PhU optimizations on $V = \Omega^{(h)} \cup \Omega'^{(h)}$ set of coherent points [see (2) and (3)]. To facilitate PhU procedures and reduce PhU errors, the local networks are calculated by first computing a CDT over the points of the second graph. The bounded arcs are those of the primary network. The spatial arcs of the secondary network, representing a spatial triangulation in the azimuth/range domain pertaining to $\Omega'^{(h)}$, can be straightforwardly identified by building up a Delaunay triangulation. A more sophisticated approach could also be applied, improving results in reduced PhU errors and solution reliability at the expense of increased computation time (see Appendix).

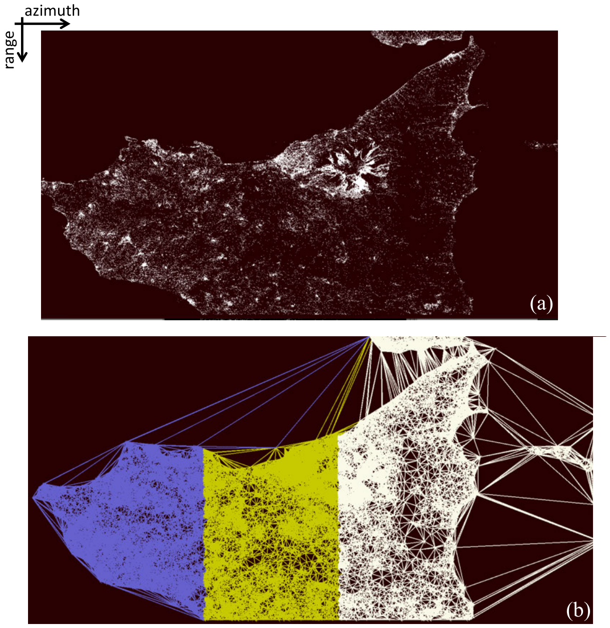

Fig. 4. Pictorial representation of tiles decomposition adopted by the developed multiscale PhU approach. (a) Map of coherent pixels retrieved at the 2 × 10 (azimuth × range) scale by processing the Sentinel-1 SAR dataset relevant to Sicily Island, Italy. (b) Three subtriangulations were computed from three sets (i.e., $Z = 3$) of nonoverlapped pixels that are represented in blue, yellow, and white, respectively.

C. Further Remarks on the Algorithm Implementation

A few additional remarks concerning the implementation of the developed PhU scheme are now in order. First, it is worth highlighting that every triangle of the primary graph determines a convex envelope whose relevant points can be independently unwrapped (as detailed in Section II-B). Accordingly, in the case that the number of points to be processed at the hth scale $\Omega^{(h)}$ exceeds a given threshold value (e.g., a few million), the secondary graph can be easily split into a series of Z subnetworks (e.g., tiles) made of several triangles of the primary graph that can independently be processed, exploiting high-performance computing (HPC) [72] and dynamic processing algorithms (e.g., [71]), as in the pictorial representation shown in Fig. 4.

Furthermore, it is interesting to note that, in a limiting condition, every triangle of the primary graph could be processed independently. Indeed, in contrast to other PhU methods for unwrapping large swath interferograms that are based on splitting and reassembling the PhU solutions using spatially overlapped tiles that are not generally spatially consistent,

---

[2] Generally, SBAS [11] or any other temporal InSAR methodology [10], [47] can be used to compute the phase vector $\mathbf{\Phi}^{(\mathbf{h})}$.

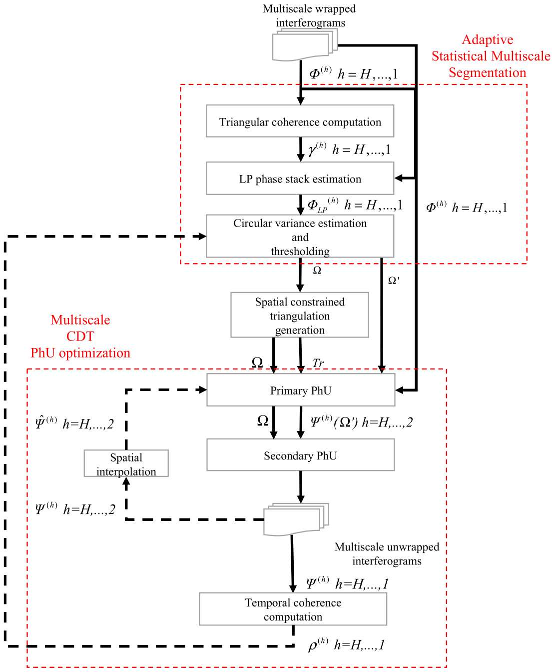

Fig. 5. Flowchart of the proposed adaptive multigrid PhU approach.

in our case a global PhU solution is available and guides PhU operations performed locally. In view of this, the adopted segmentation and network-constrained PhU scheme does not require the application of sophisticated operations to make the different tiles consistent when mosaicked.

Accordingly, the proposed method is intrinsically applicable for parallel PhU computing, generating local (high resolution and low spatial coverage) and regional/continental (shallow resolution and very extended spatial coverage) ground deformation maps and relevant products.

The block diagram of the developed multiscale PhU scheme for processing large swath multitemporal differential SAR interferograms is shown in Fig. 5. The adopted scheme assumes that the operations performed at the finest grid (i.e., $h = 1$) require the preliminary (global) PhU solutions computed at all coarser grids up to the coarsest (H-th) resolution scale. This process resembles the ascent visiting order of the V-cycles discussed in the work of Pritt [19]. At the highest scale (coarsest and low spatial sampling), a standard MCF PhU problem is solved (or generally, any other equivalent L_p PhU method could be solved, also including space-time 3-D or hybrid 2-D + 2-D PhU technique). Subsequently, the V-cycle is visited in descending order, from the highest (coarsest, low spatial sampling) to the lowest (finest and high spatial sampling) grid, and the PhU solutions at higher grids (global solutions) are mapped into lower grids (local grids) until the first scale is processed. We finally remark that the developed PhU scheme is modular and, therefore, it can be used to unwrap even a subset of the whole coherent points identified at the distinctive scales and focus on specific regions of interest with no need to unwrap the whole set of coherent points at the finer scales.

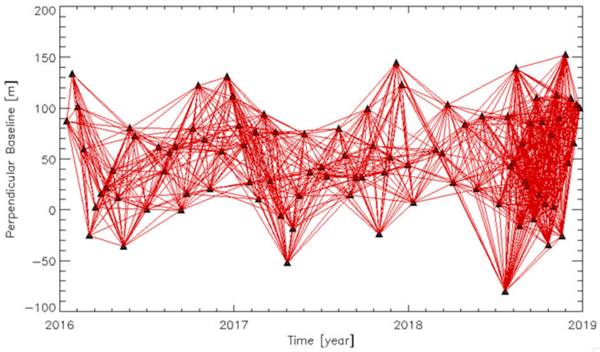

Fig. 6. Selected short baseline data pairs (red arcs) generated from Sentinel-1 SAR data (black triangles) related to the Central Valley test area.

V. EXPERIMENTAL RESULTS

In this section, we apply the developed multiscale PhU method to two SAR datasets in the U.S. and Italy, and we test experimentally the efficiency of the segmentation and unwrapping procedures.

A. Central Valley Case Study

The first dataset consists of 92 SAR images of the Central Valley of California, U.S., collected by the European Copernicus Sentinel-1A/B SAR sensors from January 14, 2016 to December 23, 2018 (ascend ing orbits, Path 137). Three sequences of 1056 short baseline differential SAR multilooked SAR interferograms were generated from this set of SAR images, selected by imposing a maximum temporal baseline of 144 days. We considered three distinctive spatial scales with 4 × 20, 8 × 40, and 16 × 80 looks (azimuth × range), respectively. The distribution of the used SAR images in the temporal/perpendicular baseline plane as well as the identified network of short baseline InSAR data pairs are shown in Fig. 6. For the interferogram generation [41], [42], precise satellite orbit information and the one-arc-second shuttle radar topography mission (SRTM) digital elevation model (DEM) of the region were used to remove the topographic phase contributions from the interferograms. To illustrate the effectiveness of the developed multiscale PhU method, we first applied the adaptive, statistical segmentation approach described in Sections III and IV and identified, at the three selected scales, the relevant group of coherent SAR pixels, where the developed constrained network PhU optimization procedure was subsequently applied. Fig. 7 portrays the masks of coherent SAR pixels at the scales (a) 16 × 80, (b) 8 × 40, and (c) 4 × 20, highlighting those of the primary and secondary graphs of the constrained-network-based PhU strategy.

The number of coherent SAR points at the given scales is also pictorially represented through the histograms shown in Fig. 8. The two higher spatial resolution sets (8 × 40 and 4 × 20 scales) of multitemporal, multilooked SAR interferograms have sequentially been unwrapped by the method detailed in Sections III and IV.[3] The mean ground deformation velocity

---

[3] To increase the number of detectable points, the interferograms are first unwrapped on sparse grids of coherent SAR points and then spatially interpolated to get the unwrapped phases in correspondence with all pixels of the imaged scene.

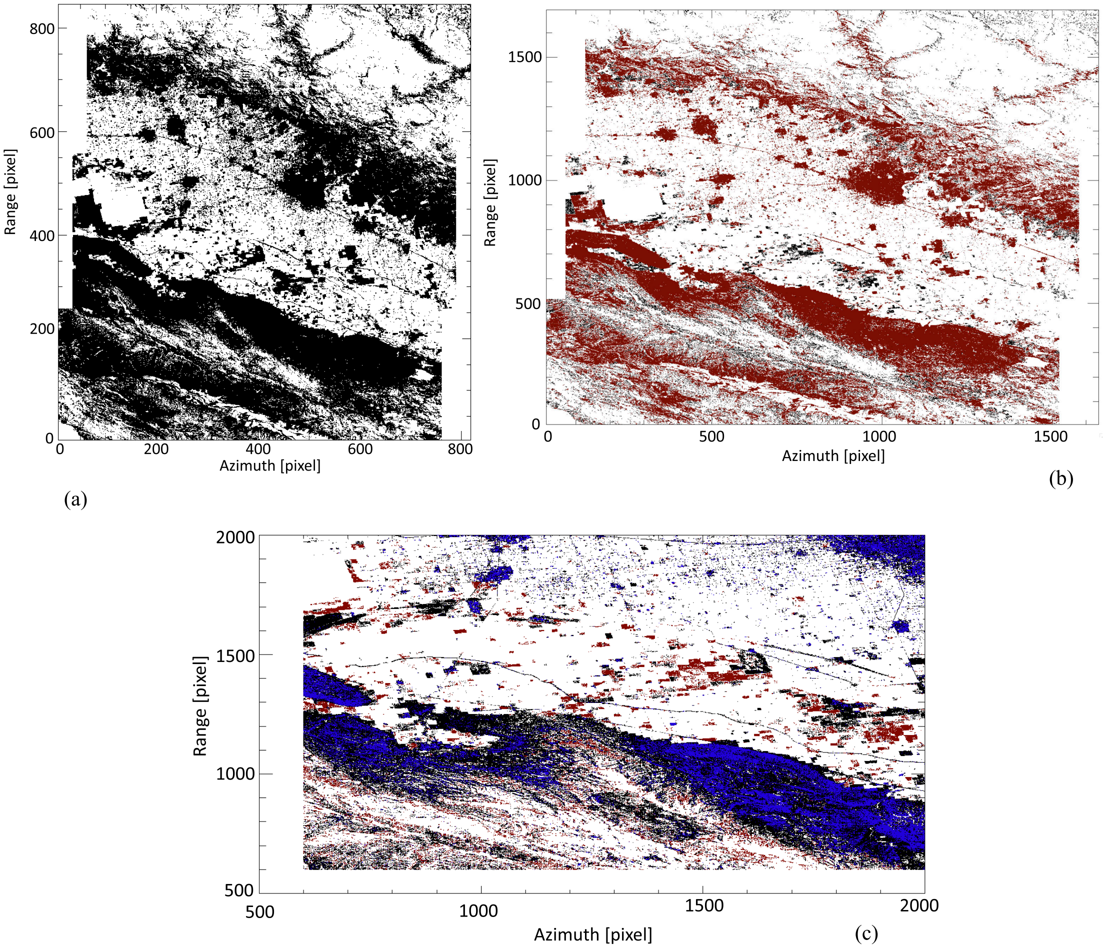

Fig. 7. Coherent SAR pixels at scales at (a) 16 × 80, (b) 8 × 40, and (c) 4 × 20, highlighting primary and secondary points in black and red, respectively, in (b) and (c). The mask at the 4 × 20 scale zoomed-in view on an area in the central part of the Central Valley. The blue points are those of the very coherent set of points for which the phase is well constrained by the PhU at higher scales.

maps and the time series of ground deformations were computed at the three inherent scales by processing the sequences of unwrapped multilooked SAR interferograms with the small baseline subset (SBAS) [11] technique.[4]

Fig. 9(a) shows the velocity ground deformation map at the coarser scale (16 × 80), where only the coherent points that exhibit a temporal coherence value larger than 0.7 are depicted on the map. Specifically, to appreciate the benefits of the improved spatial resolution at this scale, in Fig. 9(b), we focus on the patch at 4 × 20 scale highlighted by the rectangular box overlaid on the map of Fig. 9(a). Time series plots for two points in Fig. 9(b) are shown. Significant subsidence at II has been identified previously using L-band UAVSAR data [75]. We also show in Fig. 9(c) and (d) the maps of the ground deformation velocity differences between the scales 16 × 80–8 × 40 and 8 × 40–4 × 20. We further remark that the adopted multiscale PhU method is paramount since it allows not only unwrapping large swath interferograms efficiently, as further confirmed by the analysis of the algorithm computational burden detailed in Section VI, but also to automatically discovering and highlighting specific ground deformation signals that are characteristic of a determined spatial scale. This kind of analysis can be definitely improved, and help identify and recover "hidden" signals in multiscale sequences of deformation time series, for instance, with tools based on machine learning (ML) for anomaly detection with multiple time series [76], [77], [78], [79], [80].

B. Italy Case Study

We also applied the developed PhU multiscale scheme to a time series of 34 C-band SAR images acquired by the Sentinel-1A instrument from January 6, 2023 to February 6, 2024, with ascending passes (Path 44). The investigated area extends for approximately 1000 × 300 km and covers most of the Peninsula of Italy, from Sicily to the Alps. Fig. 10 shows the distribution of the used SAR data in the temporal/perpendicular baseline plane and the set of $M = 330$ InSAR data pairs selected by imposing a maximum interferometric temporal baseline of 144 days.

---

[4] The atmospheric phase screen (APS) contributions have properly been estimated and compensated for using the method implemented in SBAS, also complemented with the approach proposed in [73]. The (wrapped) interferograms were also preliminarily processed to correct the systematic bias components evidenced in [74] which however were rather limited since we selected and exploited interferograms with a relatively high temporal baseline (e.g., we imposed a maximum temporal baseline of 144 days).

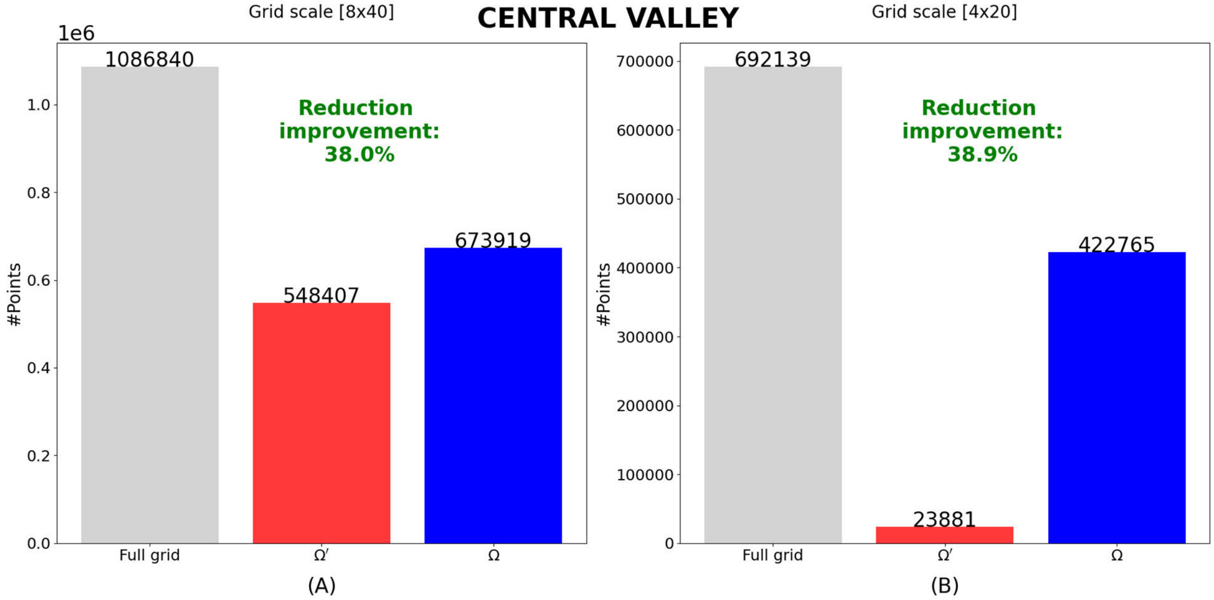

Fig. 8. Histograms of number of points identified at (a) 8 × 40 and (b) 4 × 20 scales, respectively. The histograms in gray account for the number of coherent points satisfying $\{P : \gamma^{(h)}(P) \geq 0.7\}$, whereas those in red and blue for the groups of ω' and ω'. The reduction improvement is given by the decrease percentage of the coherent points between histograms in blue and gray.

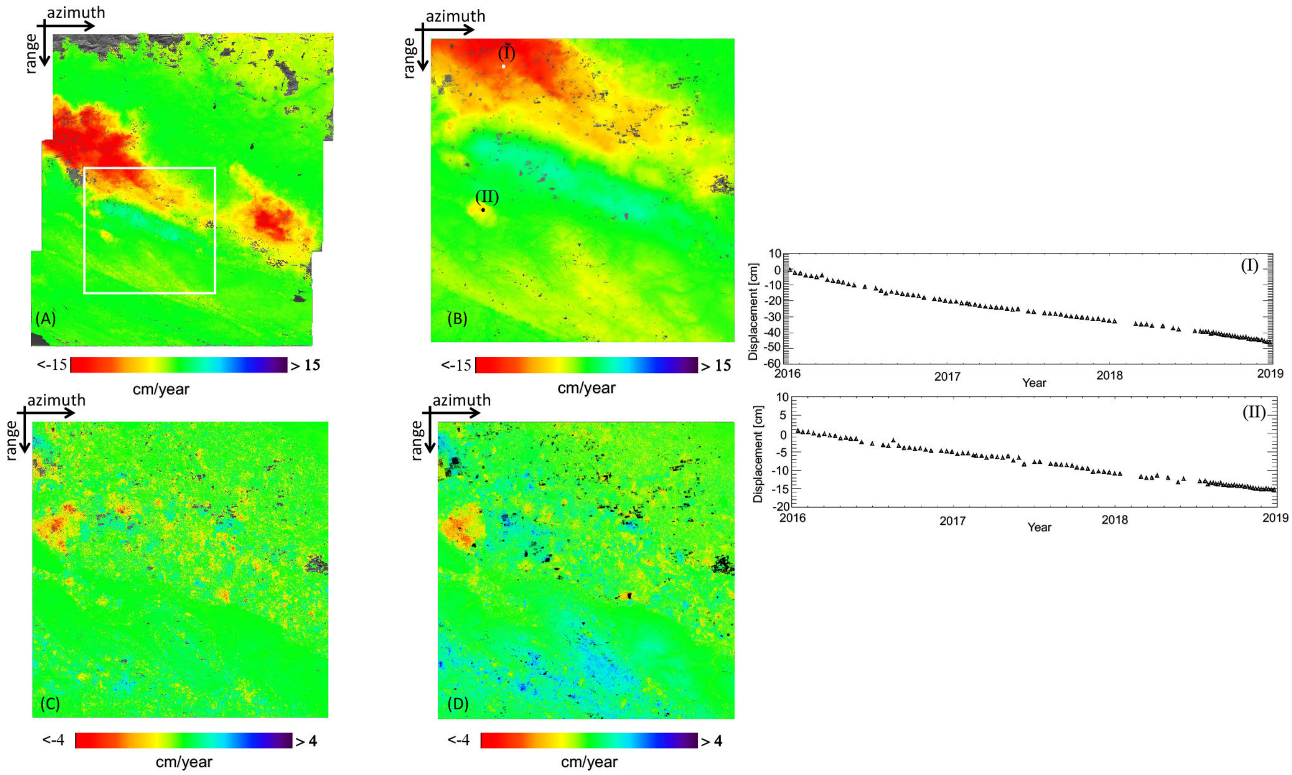

Fig. 9. (a) Mean ground deformation velocity map at 16 × 80 scale for Central Valley area. (b) Zoomed-in view at 4 × 20 scale of the area highlighted by the white box in (a). (c) and (d) Mean ground deformation velocity difference between the (16 × 80 and 8 × 40) and (8 × 40 and 4 × 20) scales, respectively. (I) and (II) Time series of ground deformation of two selected pixels in the zoomed-in view area (b). 4 × 20, 8 × 40, and 16 × 80 correspond to 3292 × 3388, 1646 × 1694, and 823 × 847 pixels in azimuth and range, respectively.

Four sets of multiscale, multilooked differential SAR interferograms were generated considering the multilook factors of (azimuth × range) 16 × 80, 8 × 40, 4 × 20, and 2 × 10. As an example, we show in Fig. 11(a), a selection of three differential SAR interferograms of the area with temporal baselines of (a) 12 days, (b) 48 days, and (c) 144 days.

By applying the PhU methods described in Sections III and IV, we processed the relevant four stacks of interfero-

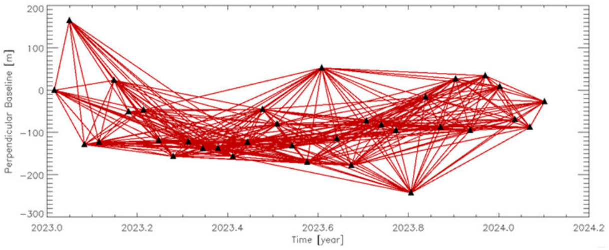

Fig. 10. Selected short baseline data pairs (red arcs) generated from Sentinel-1A SAR data (black triangles) related to the Italy test area.

grams. The number of coherent SAR pixels involved in the PhU operations at the four distinctive resolution scales is displayed through the histograms in Fig. 12.

The generated stacks of unwrapped interferograms were then inverted through the SBAS approach [11], [35] to retrieve the mean ground deformation velocity map of Italy at the different scales. Fig. 13(a) shows the ground deformation velocity map related to the coarser scale (i.e., 16 × 80) superimposed on an amplitude map of the area. Only SAR pixels characterized by a temporal coherence greater than 0.7 are displayed in this map. The map of the temporal coherence at the 16 × 80 scale is shown in Fig. 13(b). Note that the PhU operations have exclusively been performed at the coarser scale by applying the extended MCF (E) approach, followed by the PhU correcting step described in [27]. The subsequent PhU operations at the remaining scales have then been performed as detailed in Sections II and III. Specifically, Fig. 13(c) shows the map of the circular variance between the 16 × 80 and 8 × 40 wrapped phases. The pixels in red highlight the coherent zones where the phase circular variance is low. This map is used to adaptatively identify the pixels at the 8 × 40 scale where constrained PhU operations (considering both the constrained and unconstrained points) are subsequently performed. Several spot areas characterized by significant deformation patterns can be seen at the national scale, and especially the areas nearby Mt. Etna, Sicily Island, and the zone of the Phlegraean fields caldera along the Southern coast of Italy in the vicinity of the city of Naples. These areas are known to be currently affected by ground deformation episodes linked to the Mt. Etna eruptions in Sicily and the on-going phenomenon of bradyseism in the Phlegraean Fields caldera. To make evident the deformation signals at the finer scale, we show in Fig. 14(a) the map of the mean ground deformation velocity of the Phlegraean Fields caldera and surrounding area, respectively. We also show in Fig. 15 the map of the ground deformation difference between the 8 × 40 and 4 × 20 scales to highlight the areas where local anomalies are present. We observe that 9.41% of the coherent pixels identified at the 4 × 20 scale considering the circular variance metrics are effectively located in areas where the ground deformation difference between the neighboring scales 8 × 40 and 4 × 20 is larger than 10 mm/year. Finally, as representative of the deformation pattern of the entire area, we plot the ground deformation time series of three selected points located in the caldera region, see Fig. 14(I)–(IV). The geological analyses of these ground deformation products as well as their implications for the management of the risk conditions in the area are in progress and, however, are outside the scope of the study reported here.

VI. ALGORITHM PERFORMANCE ANALYSIS

Section VI provides readers with some observations related to the computational burden of the developed multiscale PhU method. In particular, the analysis of the computational cost of the PhU scheme is provided considering the three different (macro) processing steps that compose the method detailed in Sections III and IV and outlined in Fig. 5.

A. Multiscale Segmentation Procedure

The implemented procedure recursively moves from the coarsest ($h = H$) to the finest ($h = 1$) scale. The workload during each recursion on every grid directly correlates with the total number of (coherent) SAR points at the finest scale, namely, q, as it applies to each subprocess: 1) interpolation; 2) triangular coherence determination; and 3) circular variance estimation. Since the number of points at each grid is approximately a constant fraction of that of the next finer grid (one-fourth), it can be demonstrated that the computational complexity of the implemented multiscale segmentation (quadtree-like) is as follows:

$$C_{\mathrm{MS}} = O\left(\sum_{h=1}^{H} 2M \cdot \frac{q}{2^{2(h-1)}}\right) \cong O\left(\frac{M \cdot q}{6} \cdot \left(1 - 2^{-2H}\right)\right). \tag{15}$$

Indeed, most of the computational cost of the segmentation algorithm is linked to the interpolation processes of the M-wrapped interferograms performed whilst moving between neighboring scales (e.g., from $h + 1$ to h), see (6). This cost strictly depends on the number of points, namely, $q_h = (q/2^{2(h-1)})$, at the generic h th scale, and for a bilinear interpolator [81] is of about $O(2M \cdot q_h)$, where the factor 2 is due to the fact that the sine and cosine components of the complex signal $\exp(j\phi_k^{(h+1)})$ must be separately interpolated. Hence, (15) is derived by summing up the costs for the interpolation procedures performed at the different resolution scales, considering globally negligible costs for the calculation of the maps of circular variance and triangular coherence, which permit identifying the coherent points at every scale.

B. Spatial Triangulations and CDT Generation

The investigation of optimal triangulations for a set of points q in a plane was the subject of extensive research in computational geometry [82]. It is one of the most longstanding open problems in the literature on the subject [83], and various optimality criteria have been explored, among which the weight (e.g., Euclidean distance) of each arc stands out as one of the most prominent [84], [85].

Considering the weights defined by (14), in this work, we applied a solution based on a CDT [86], whose computational cost is

$$C_{\mathrm{TR}} = O(m \log(m)) \tag{16}$$

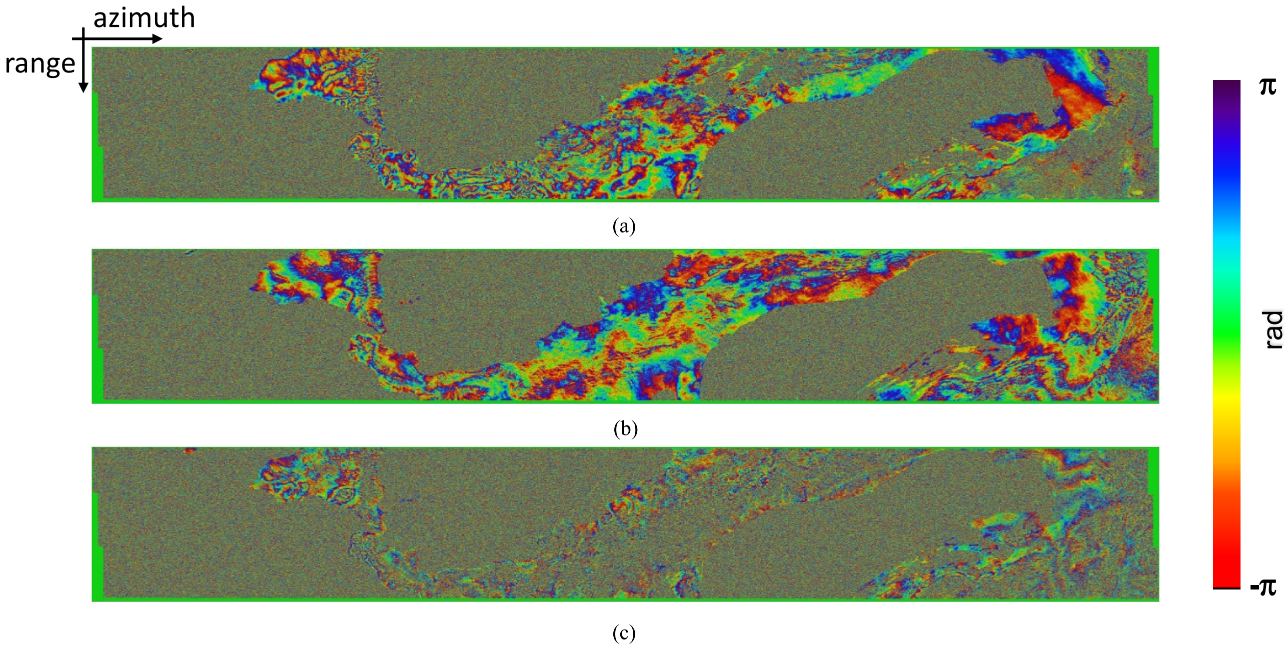

(a)

(b)

(c)

Fig. 11. Selection of three differential interferograms of the Italy area relevant to the SAR data pairs collected on (a) January 1, 2024 and January 13, 2024 (12 days), (b) December 20, 2023 and February 1, 2024 (48 days), and (c) September 15, 2023 and February 6, 2024 (144 days). The interferograms scale is 16 × 80, which corresponds to 6023 × 867 pixels in azimuth and range.

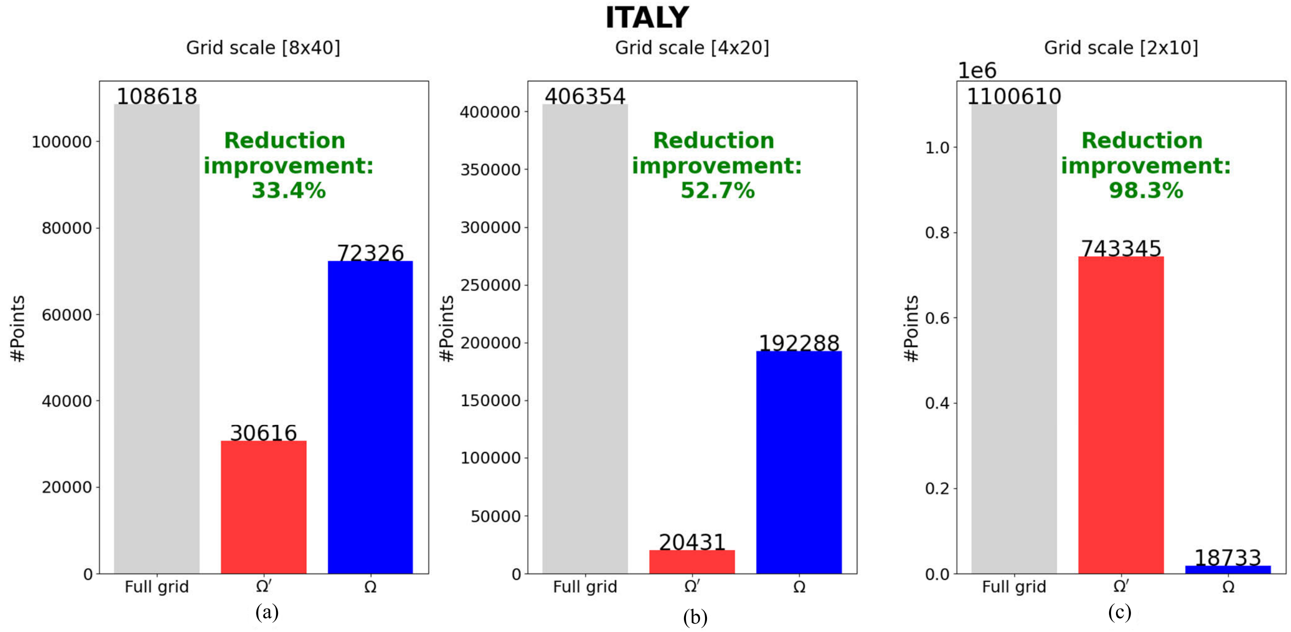

(a) (b) (c)

Fig. 12. Histograms of number of points identified at (a) 8 × 40, (b) 4 × 20, and (c) 2 × 10 scales, respectively. The histograms in gray account for the number of coherent points satisfying $\{P : \gamma^{(h)}(P) \geq 0.7\}$, whereas those in red and blue for the groups of ω' and ω'. The reduction improvement is given by the decreased percentage of the coherent points between histograms in blue and gray.

where m indicates the set of potential nonintersecting spatial arcs that must be scanned while the minimum weight triangulation is computed using a Greedy approach.

C. Multiscale PhU Operations

As described in Section IV, the developed multiscale optimization consists of different constrained network PhU operations performed at the primary and secondary graph levels. Let us consider the finest resolution scale and let q be the number of coherent points identified at this scale. The spatial (optimal) triangulation computed starting from these q points is composed (worst case) of $q - 2$ triangles and $(3q - 6/2)$ nonintersecting connecting arcs. Assuming the PhU operations of the selected M differential SAR interferograms are performed using MCF-oriented solvers, the required computational cost can be inferred considering that the MCF solution relies on a relaxation approach and, in the worst case,

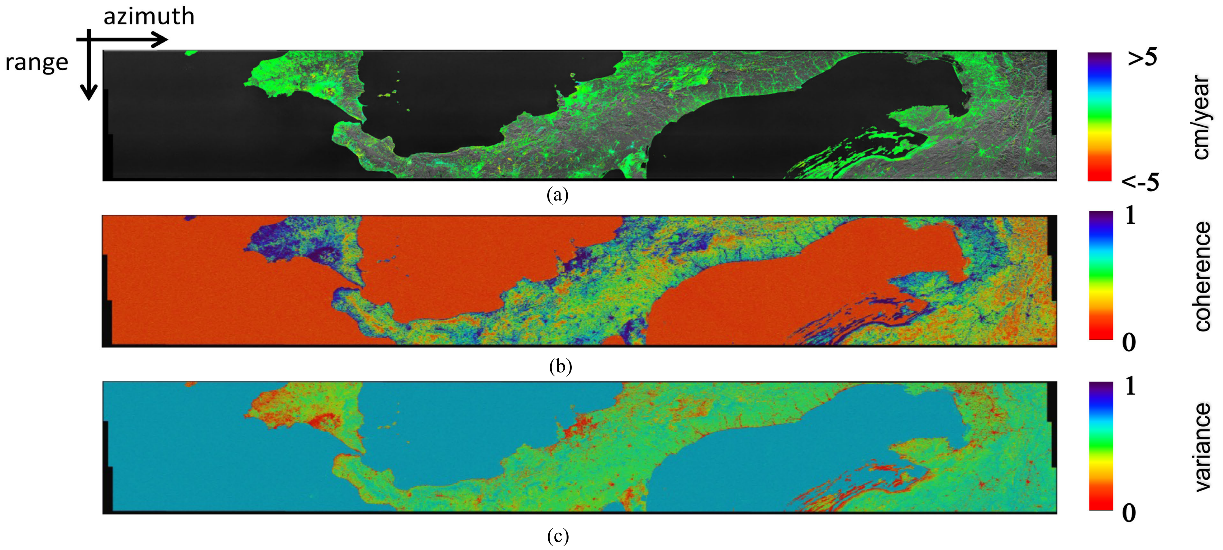

Fig. 13. (a) Mean ground deformation velocity map at the 16 × 80 scale superimposed to an amplitude map of the area. (b) Temporal coherence map and (c) circular variance map between 16 × 80 and 8 × 40 scales. The 16 × 80 scale corresponds to 6023 × 867 pixels in azimuth and range.

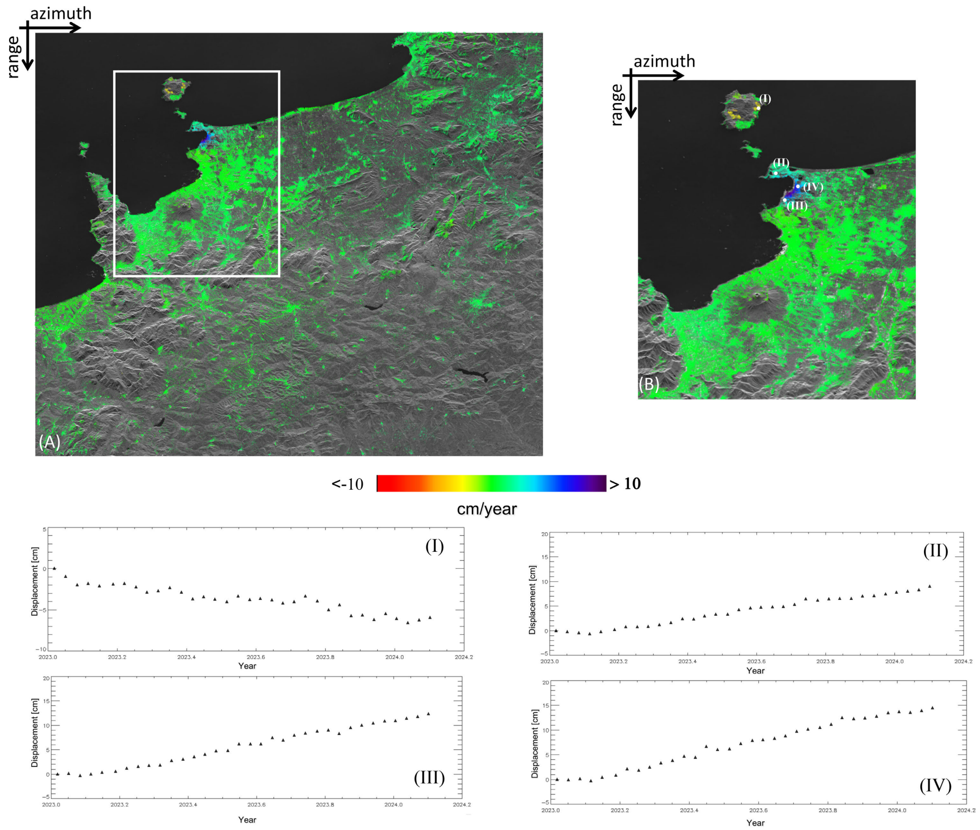

Fig. 14. (a) Mean ground deformation velocity map at 2 × 10 scale. (b) Zoomed-in view of the region highlighted by the white box in (a). (I)–(IV) Time series of ground deformation for the points labeled as (I)–(IV) in (b). The 2 × 10 scale corresponds to 48 188 × 6942 pixels in azimuth and range.

the cost of relaxations is given by [63] and [65]

$$C_M = O\left(Mnm^2CU^2\right) \cong O\left(9q^3MCU^2\right) \tag{17}$$

where $n = q - 1$ and $m = 3q - 6$ are the number of nodes and arcs of the equivalent networks, U is the MCF network arcs capacity, and C is the maximum cost of the MCF network arcs.

Splitting the PhU operations over the (primary) graph into a series of Z independent operations performed on corresponding nonoverlapping Z tiles (e.g., see Fig. 4), which are composed of $(q/Z) - 1$ triangles and $3(q/Z) - 6$ arcs, the computational cost of the PhU operations[5] performed over M SAR interferograms is

$$C_{M,Z} = O\left(ZM\left(\frac{q}{Z} - 1\right)\left(3\frac{q}{Z} - 6\right)^2 CU^2\right). \tag{18}$$

---

[5] For the sake of simplicity, we assume that MCF operations are performed independently using 2-D approaches. However, an additional cost has to be considered when 3-D [22] or hybrid 2-D+2-D [23], [24] PhU approaches are used.

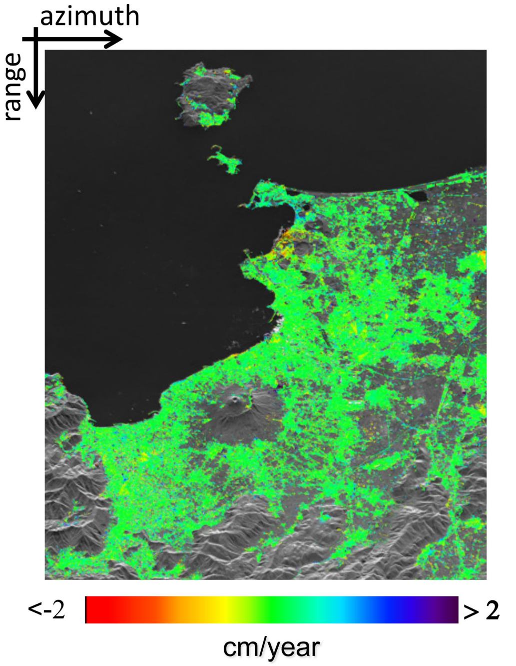

Fig. 15. Map of the ground deformation difference between the 8 × 40 and 4 × 20 scales for the area highlighted with the white box in Fig. 14(a). 8 × 40 and 4 × 20 scales correspond to 12 047 × 1735 and 24 094 × 3471 pixels in azimuth and range, respectively.

However, the adopted network-constrained PhU solution also requires knowledge of the unwrapped phases relevant to the primary graph points derived from the neighbor (coarser) spatial resolution grid. This operation has an additional computational cost. Considering that neighbor scales have (in our worst case) one-fourth of the coherent points, this cost is

$$C_{M,V} = O\left(M\left(\frac{q}{4}-1\right)\left(3\frac{q}{4}-6\right)^2 CU^2\right). \tag{19}$$

Our adopted PhU scheme consists of the solution of an MCF problem at the coarsest spatial grid, i.e., $h = H$, followed by a series of constrained network optimizations over the remaining $H-1$ spatial resolution scales. Considering the implementation of an MCF-oriented PhU optimization described in Section II, the adopted strategy consists of solving the problem by generating a CDT and simply imposing that the cost of constrained arcs $\mu_c = L$ are much larger than the cost of the unconstrained arcs $\mu_u = w_q = w, \forall q$ [see (3a)] where w_q is the weight of the q th edge of the computed CDT. Considering this implementation of the problem, the total computational cost of the method is

$$\begin{aligned} C_{\text{total}} &= \sum_{h=1}^{H} C_{M,V}^{h} \\ &= O\left(\sum_{h=1}^{H-1} MZ(q_h-1)\left(\frac{3}{2}(q_h-2)\right)^2 \frac{\mu_c}{\mu_u} CU^2\right) \\ &\quad + O\left(\frac{9}{4} M q_H Z (q_H Z-2)^2 CU^2\right) \end{aligned} \tag{20}$$

where $q_h = (q/z \cdot 2^{2(h-1)})$ is the total number of SAR pixels in a tile of the hth spatial resolution scale.

Note that the PhU operations related to the coarser resolution scale are directly performed on the total number of points at the H-scale (i.e., $(q/2^{2(h-1)}) = Z \cdot q_H$), with no tiling operations, and accordingly, the last term of (20) accounts for the computational cost of these operations. After some trivial mathematic manipulations and considering $q_h = (q/Z \cdot 2^{2(h-1)}) >> 1, \quad h = 1, \ldots, H$, (20) simplifies as follows:

$$\begin{aligned} C_{\text{total}} &= O\left\{9M \cdot \frac{\mu_c}{\mu_u}\frac{q^3}{Z^2} CU^2 \left[\frac{2^{-6}-2^{-6H}}{1-2^{-6}}\right]\right\} \\ &\quad + O\left(9M \cdot \frac{q^3}{2^{6H}} CU^2\right). \end{aligned} \tag{21}$$

As a further remark, we observe that as the number of scales increases, the computational cost of the MCF operations performed at the coarsest resolution scale becomes rapidly irrelevant; accordingly, the total computational cost of the algorithm can be approximated as follows:

$$\begin{aligned} C_{\text{total}} &= O\left\{9M \cdot \frac{\mu_c}{\mu_u} \cdot \frac{q^3}{Z^2 \cdot 2^6} CU^2\right\} \\ &= O\left\{9q^3 MCU^2 \left(\frac{1}{Z^2} \cdot \frac{\mu_c}{\mu_u} \cdot 2^{-6}\right)\right\} \\ &= \left(\frac{\mu_c}{\mu_u} \cdot \frac{2^{-6}}{Z^2}\right) C_M. \end{aligned} \tag{22}$$

Equation (22) demonstrates that the total computational cost does not depend significantly on the number of resolution scales, H, even though the coarser scales are fundamental to recovering reliable global PhU solutions and avoiding the tile recombination problems of the alternative solutions to solve the problem of unwrapping large swath interferograms [35], [49].

Fig. 16(a) and (b) shows the trends of the computational costs for the PhU using MCF [see (17)] and the multitile solution [see (18)]. Fig. 16(a) shows the dependence of the MCF cost with q^3. Using a tiling approach, the trend becomes proportional to Z^2 as shown in Fig. 16(b).

More importantly, (22) shows that the multiscale PhU method efficiency (worst case) is equal to

$$\varepsilon = \frac{C_M}{C_{\text{total}}} = 2^6 \cdot Z^2 \cdot \frac{\mu_u}{\mu_c} \tag{23}$$

which is plotted in Fig. 16(c) where we considered a value of $\mu_c/\mu_u = 10^2$, which has been shown experimentally to be sufficient to guarantee reliable (constrained) unwrapped results. Note that in the case that the constrained PhU problems were solved with selected slice numbers equal to $Z = 2^r, \quad r = 0, 1, 2, \ldots$ the algorithm efficiency would be $\varepsilon = 0.01 \cdot 2^{(2r+6)}$.

Finally, it is worth remembering that (23) refers to a sequential implementation of the developed multiscale PhU method, and, as expected, the efficiency is higher if more tiles are used [see Fig. 16(c)]. However, the developed PhU scheme can automatically and straightforwardly be implemented considering dynamic processing adaptations. Indeed, every single tile at each resolution scale can independently be processed in parallel on different machines, except for the solution of the MCF problem at the coarsest scale [which, however, has a reduced cost because the number of pixels

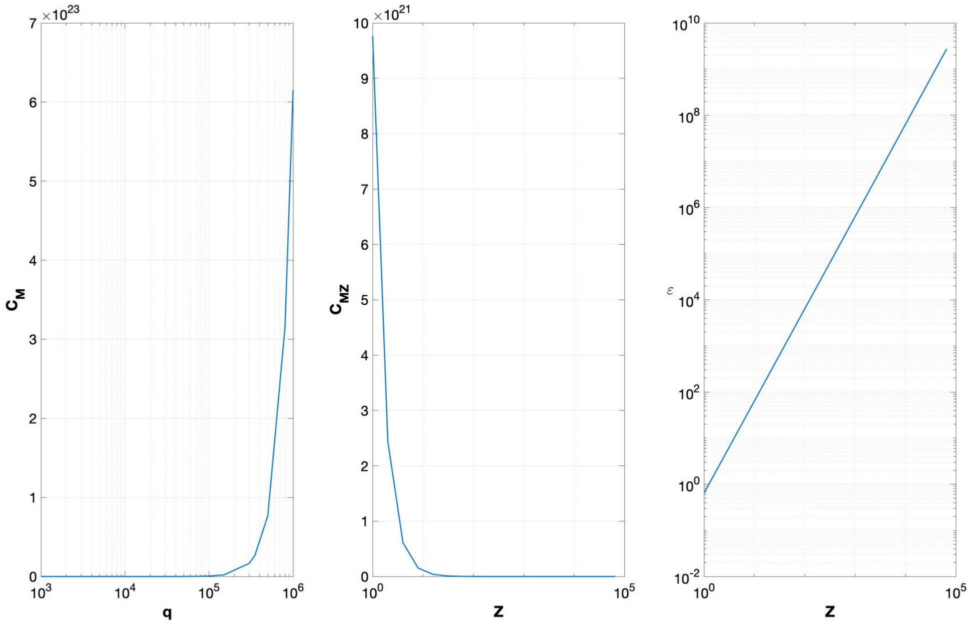

(a) (b) (c)

Fig. 16. PhU computational cost using (a) MCF relaxation-based approach and (b) multiscale. (c) Efficiency of the proposed method. Note that, q and z are the number of coherent points identified and the number of nonoverlapping tiles at each scale.

at that scale is in the order of $q/2^{(H-1)}$]. Accordingly, the efficiency of the implementation of our developed PhU scheme on multicore/multithread architectures is expected to dramatically increase. This is a matter for further extended investigations.

VII. CONCLUSION

In this work, we have proposed a solution for processing large-swath SAR interferograms. By leveraging statistical properties and multiscale decomposition, the presented method provides an efficient and reliable strategy to efficiently unwrap sequences of SAR interferograms that cover vast terrain areas with a dense grid of points. The proposed method proved crucial in efficiently processing large swaths of InSAR data, as validated by the computational cost analysis provided in Section VI as well as by the experiments shown in Section V. The method is also capable of identifying and highlighting distinctive ground deformation patterns that occur at specific spatial scales. This PhU scheme is particularly attractive given the prospect of new sensors such as the L-band NASA-ISRO SAR (NISAR) that will enable the monitoring of vast areas of the Earth's surface, with an enhanced number of measurement points corresponding to detectable targets on the ground, with global and rapid coverage, and providing unprecedented opportunities for disaster response, and damage mitigation and assessment.

In this context, the approach proposed in this article may be very relevant for developing advanced, rapid, and efficient interferometric processing approaches, thereby playing a pivotal role in tracking individual physical processes responsible for deformation and providing a new effective operational strategy for managing and mitigating risks using InSAR.

APPENDIX

This Appendix deals with the description of a sophisticated approach for the generation of a CDT to be used during multiscale PhU operations presented in Section IV. It consists of searching for a spatial triangulation whose arcs satisfy the following conditions: 1) the vector of phase gradients computed over the arcs is less dispersed than its average value and 2) the estimated ground deformation rates and residual topography over the spatial triangulation arcs are minimal. By referring to the generic spatial arc that connects the pixels labeled as A and B, the condition 1) is determined by computing the circular variance of the wrapped phase gradients

$$\mathrm{Var}_{AB} = 1 - \frac{1}{\mathrm{Tr}}\left|\sum_{k=1}^{\mathrm{Tr}} \exp\left[j\left(\phi_{\mathrm{Tr},k}^{(h)}(B) - \phi_{\mathrm{Tr},k}^{(h)}(A)\right)\right]\right| \times (\Delta v_{AB}, \Delta z_{AB}) \qquad (\mathrm{A.1.1})$$

that maximize the value of Γ_{AB}

$$\begin{aligned}(\Delta v_{AB}, \Delta z_{AB}) &= \operatorname{argmax} \\ &\times \left\{\Gamma_{AB} = \frac{1}{M}\left|\sum_{k=1}^{M} \exp\left[j\left(\Delta\phi_{k,AB}^{(h)} - \frac{4\pi}{\lambda}\cdot\Delta t_k\cdot\Delta v_{AB}\right.\right.\right.\right. \\ &\qquad \left.\left.\left.\left. - \frac{4\pi}{\lambda}\cdot\frac{\Delta b_k}{R\cdot\sin\vartheta}\Delta z_{AB}\right)\right]\right\}\right. \end{aligned} \qquad (\mathrm{A.1.2})$$

where $\Delta\phi_{k,AB}^{(h)} = \phi_k^{(h)}(B) - \phi_k^{(h)}(A)$, Δv_{AB} and Δz_{AB} are the deformation rate and the topography over the arc connecting the points A and B, λ is the sensor operational wavelength, R is the sensor-to-target (slant range) distance, and ϑ is the incidence angle of the transmitted electromagnetic waves on the ground. The triangulation of the secondary network is eventually achieved by considering the set of spatial arcs that satisfy the condition $\varsigma = \{AB : \Gamma_{AB} \geq \eta \cap \Lambda_{AB} \leq \mu\}$, with (η, μ) selected thresholds, and searching for the greedy triangulation [83], [84], [85] that minimizes the following metric:

$$\mathrm{Tr} = \operatorname{argmin}\left\{\sum_{\varepsilon}\left(\frac{|\Delta v_{AB}|}{|\Delta v_{\max}|} + \frac{|\Delta z_{AB}|}{|\Delta z_{\max}|}\right) + \Lambda_{AB}(1 - \Gamma_{AB})\right\}. \tag{A.1.3}$$

The problem described by (14) is a classical problem of searching for a minimum weighted triangulation (MWT) for which sequential and efficient parallel implementations are available in the literature [83], [84], [85].

ACKNOWLEDGMENT

Sentinel-1 data, courtesy of the European Space Agency (ESA), were downloaded from the Alaska Satellite Facility (http://www.asf.alaska.edu). The digital elevation model (DEM) of the investigated zones was acquired through the Shuttle Radar Topography Mission (SRTM) archive.

REFERENCES

[1] A. K. Gabriel, R. M. Goldstein, and H. A. Zebker, “Mapping small elevation changes over large areas: Differential radar interferometry,” *J. Geophys. Res., Solid Earth*, vol. 94, no. 7, pp. 9183–9191, Jul. 1989, doi: 10.1029/jb094ib07p09183.

[2] Y. Fialko and M. Simons, “Deformation and seismicity in the coso geothermal area, inyo county, california: Observations and modeling using satellite radar interferometry,” *J. Geophys. Res., Solid Earth*, vol. 105, no. B9, pp. 21781–21793, Sep. 2000, doi: 10.1029/2000jb900169.

[3] H. A. Zebker, P. A. Rosen, and S. Hensley, “Atmospheric effects in interferometric synthetic aperture radar surface deformation and topographic maps,” *J. Geophys. Res., Solid Earth*, vol. 102, no. 4, pp. 7547–7563, Apr. 1997, doi: 10.1029/96JB03804.

[4] M. Manzo et al., “Surface deformation analysis in the Ischia Island (Italy) based on spaceborne radar interferometry,” *J. Volcanol. Geothermal Res.*, vol. 151, no. 4, pp. 399–416, Mar. 2006, doi: 10.1016/j.jvolgeores.2005.09.010.

[5] G. Liu et al., “Surface deformation associated with the 2008 Ms8.0 wenchuan earthquake from ALOS L-band SAR interferometry,” *Int. J. Appl. Earth Observ. Geoinf.*, vol. 12, no. 6, pp. 496–505, Dec. 2010, doi: 10.1016/j.jag.2010.05.005.

[6] Z.-K. Shen et al., “Slip maxima at fault junctions and rupturing of barriers during the 2008 wenchuan earthquake,” *Nature Geosci.*, vol. 2, no. 10, pp. 718–724, Oct. 2009, doi: 10.1038/ngeo636.

[7] A. Simms, L. C. Reynolds, M. Bentz, A. Roman, T. Rockwell, and R. Peters, “Tectonic subsidence of California estuaries increases forecasts of relative sea-level rise,” *Estuaries Coasts*, vol. 39, no. 6, pp. 1571–1581, Nov. 2016, doi: 10.1007/s12237-016-0105-1.

[8] A. H.-M. Ng, L. Ge, and X. Li, “Assessments of land subsidence in the Gippsland basin of Australia using ALOS PALSAR data,” *Remote Sens. Environ.*, vol. 159, pp. 86–101, Mar. 2015, doi: 10.1016/j.rse.2014.12.003.

[9] Q. Zhao et al., “A DInSAR investigation of the ground settlement time evolution of ocean-reclaimed lands in Shanghai,” *IEEE J. Sel. Topics Appl. Earth Observ. Remote Sens.*, vol. 8, no. 4, pp. 1763–1781, Apr. 2015, doi: 10.1109/JSTARS.2015.2402168.

[10] A. Ferretti, C. Prati, and F. Rocca, “Permanent scatterers in SAR interferometry,” *IEEE Trans. Geosci. Remote Sens.*, vol. 39, no. 1, pp. 8–20, Jan. 2001, doi: 10.1109/36.898661.

[11] P. Berardino, G. Fornaro, R. Lanari, and E. Sansosti, “A new algorithm for surface deformation monitoring based on small baseline differential SAR interferograms,” *IEEE Trans. Geosci. Remote Sens.*, vol. 40, no. 11, pp. 2375–2383, Nov. 2002, doi: 10.1109/TGRS.2002.803792.

[12] C. Ojha, M. Manunta, R. Lanari, and A. Pepe, “The constrained-network propagation (C-NetP) technique to improve SBAS-DInSAR deformation time series retrieval,” *IEEE J. Sel. Topics Appl. Earth Observ. Remote Sens.*, vol. 8, no. 10, pp. 4910–4921, Oct. 2015, doi: 10.1109/JSTARS.2015.2482358.

[13] O. Mora, J. J. Mallorqui, and A. Broquetas, “Linear and nonlinear terrain deformation maps from a reduced set of interferometric SAR images,” *IEEE Trans. Geosci. Remote Sens.*, vol. 41, no. 10, pp. 2243–2253, Oct. 2003, doi: 10.1109/TGRS.2003.814657.

[14] J. M. Bioucas-Dias and G. Valadao, “Phase unwrapping via graph cuts,” *IEEE Trans. Image Process.*, vol. 16, no. 3, pp. 698–709, Mar. 2007, doi: 10.1109/TIP.2006.888351.

[15] W. Xu and I. Cumming, “A region-growing algorithm for InSAR phase unwrapping,” *IEEE Trans. Geosci. Remote Sens.*, vol. 37, no. 1, pp. 124–134, Jan. 1999, doi: 10.1109/36.739143.

[16] H. Yu and Y. Lan, “Robust two-dimensional phase unwrapping for multibaseline SAR interferograms: A two-stage programming approach,” *IEEE Trans. Geosci. Remote Sens.*, vol. 54, no. 9, pp. 5217–5225, Sep. 2016, doi: 10.1109/TGRS.2016.2558541.

[17] M. Costantini, “A novel phase unwrapping method based on network programming,” *IEEE Trans. Geosci. Remote Sens.*, vol. 36, no. 3, pp. 813–821, May 1998, doi: 10.1109/36.673674.

[18] M. D. Pritt and J. S. Shipman, “Least-squares two-dimensional phase unwrapping using FFT’s,” *IEEE Trans. Geosci. Remote Sens.*, vol. 32, no. 3, pp. 706–708, May 1994, doi: 10.1109/36.297989.

[19] M. D. Pritt, “Phase unwrapping by means of multigrid techniques for interferometric SAR,” *IEEE Trans. Geosci. Remote Sens.*, vol. 34, no. 3, pp. 728–738, May 1996, doi: 10.1109/36.499752.

[20] T. J. Flynn, “Two-dimensional phase unwrapping with minimum weighted discontinuity,” *J. Opt. Soc. Amer. A, Opt. Image Sci.*, vol. 14, no. 10, pp. 2692–2701, Oct. 1997, doi: 10.1364/josaa.14.002692.

[21] D. T. Sandwell and E. J. Price, “Phase gradient approach to stacking interferograms,” *J. Geophys. Res., Solid Earth*, vol. 103, no. 12, pp. 30183–30204, Dec. 1998, doi: 10.1029/1998jb900008.

[22] M. Costantini, F. Malvarosa, and F. Minati, “A general formulation for redundant integration of finite differences and phase unwrapping on a sparse multidimensional domain,” *IEEE Trans. Geosci. Remote Sens.*, vol. 50, no. 3, pp. 758–768, Mar. 2012, doi: 10.1109/TGRS.2011.2162630.

[23] G. Fornaro, A. Pauciullo, and D. Reale, “A null-space method for the phase unwrapping of multitemporal SAR interferometric stacks,” *IEEE Trans. Geosci. Remote Sens.*, vol. 49, no. 6, pp. 2323–2334, Jun. 2011, doi: 10.1109/TGRS.2010.2102767.

[24] A. Pepe and R. Lanari, “On the extension of the minimum cost flow algorithm for phase unwrapping of multitemporal differential SAR interferograms,” *IEEE Trans. Geosci. Remote Sens.*, vol. 44, no. 9, pp. 2374–2383, Sep. 2006, doi: 10.1109/TGRS.2006.873207.

[25] A. P. Shanker and H. Zebker, “Edgelist phase unwrapping algorithm for time series InSAR analysis,” *J. Opt. Soc. Amer. A, Opt. Image Sci.*, vol. 27, no. 3, pp. 605–612, Mar. 2010, doi: 10.1364/JOSAA.27.000605.

[26] T. Oliver-Cabrera, C. E. Jones, Z. Yunjun, and M. Simard, “InSAR phase unwrapping error correction for rapid repeat measurements of water level change in wetlands,” *IEEE Trans. Geosci. Remote Sens.*, vol. 60, 2022, Art. no. 5215115, doi: 10.1109/TGRS.2021.3108751.

[27] A. Pepe, “The correction of phase unwrapping errors in sequences of multi-temporal differential SAR interferograms,” in *Proc. IEEE Int. Geosci. Remote Sens. Symp.*, Waikoloa, HI, USA Sep. 2020, pp. 818–821, doi: 10.1109/IGARSS39084.2020.9323768.

[28] M. Lisano et al., “NASA-ISRO synthetic aperture radar (NISAR): Towards observatory-level integration and testing,” in *Proc. IEEE Aerosp. Conf.*, Mar. 2023, pp. 1–10, doi: 10.1109/AERO55745.2023.10115885.

[29] P. Kourkouli, “Chapter 9—Natural disaster monitoring using ICEYE SAR data,” in *Geoinformatics for Geosciences*, N. Stathopoulos, A. Tsatsaris, and K. Kalogeropoulos, Eds., Amsterdam, The Netherlands: Elsevier, 2023, ch. 9, pp. 163–170, doi: 10.1016/B978-0-323-98983-1.00010-7.

[30] C. W. Chen and H. A. Zebker, "Phase unwrapping for large SAR interferograms: Statistical segmentation and generalized network models," *IEEE Trans. Geosci. Remote Sens.*, vol. 40, no. 8, pp. 1709–1719, Aug. 2002, doi: 10.1109/TGRS.2002.802453.

[31] H. Yu, M. Xing, and Z. Bao, "A fast phase unwrapping method for large-scale interferograms," *IEEE Trans. Geosci. Remote Sens.*, vol. 51, no. 7, pp. 4240–4248, Jul. 2013, doi: 10.1109/TGRS.2012.2229284.

[32] K. Zhang, L. Ge, Z. Hu, A. H. Ng, X. Li, and C. Rizos, "Phase unwrapping for very large interferometric data sets," *IEEE Trans. Geosci. Remote Sens.*, vol. 49, no. 10, pp. 4048–4061, Oct. 2011, doi: 10.1109/TGRS.2011.2130530.

[33] H. Liu, M. Xing, and Z. Bao, "A cluster-analysis-based noise-robust phase-unwrapping algorithm for multibaseline interferograms," *IEEE Trans. Geosci. Remote Sens.*, vol. 53, no. 1, pp. 494–504, Jan. 2015, doi: 10.1109/TGRS.2014.2324595.

[34] L. Li, H. Zhang, Y. Tang, C. Wang, and F. Gu, "InSAR phase unwrapping by deep learning based on gradient information fusion," *IEEE Geosci. Remote Sens. Lett.*, vol. 19, pp. 1–5, 2022, doi: 10.1109/LGRS.2021.3127318.

[35] A. Pepe, L. D. Euillades, M. Manunta, and R. Lanari, "New advances of the extended minimum cost flow phase unwrapping algorithm for SBAS-DInSAR analysis at full spatial resolution," *IEEE Trans. Geosci. Remote Sens.*, vol. 49, no. 10, pp. 4062–4079, Oct. 2011, doi: 10.1109/TGRS.2011.2135371.

[36] L. Zhou, H. Yu, Y. Lan, and M. Xing, "Artificial intelligence in interferometric synthetic aperture radar phase unwrapping: A review," *IEEE Geosci. Remote Sens. Mag.*, vol. 9, no. 2, pp. 10–28, Jun. 2021, doi: 10.1109/MGRS.2021.3065811.

[37] Z. Wu, T. Wang, Y. Wang, R. Wang, and D. Ge, "Deep learning for the detection and phase unwrapping of mining-induced deformation in large-scale interferograms," *IEEE Trans. Geosci. Remote Sens.*, vol. 60, 2022, Art. no. 5216318, doi: 10.1109/TGRS.2021.3121907.

[38] F. Sica, F. Calvanese, G. Scarpa, and P. Rizzoli, "A CNN-based coherence-driven approach for InSAR phase unwrapping," *IEEE Geosci. Remote Sens. Lett.*, vol. 19, pp. 1–5, 2022, doi: 10.1109/LGRS.2020.3029565.

[39] C. Wang, X. Ding, Q. Li, and M. Jiang, "Equation-based InSAR data quadtree downsampling for earthquake slip distribution inversion," *IEEE Geosci. Remote Sens. Lett.*, vol. 11, no. 12, pp. 2060–2064, Dec. 2014, doi: 10.1109/LGRS.2014.2318775.

[40] J. M. Huntley, "Three-dimensional noise-immune phase unwrapping algorithm," *Appl. Opt.*, vol. 40, no. 23, pp. 3901–3908, Aug. 2001, doi: 10.1364/ao.40.003901.

[41] R. M. Goldstein, H. A. Zebker, and C. L. Werner, "Satellite radar interferometry: Two-dimensional phase unwrapping," *Radio Sci.*, vol. 23, no. 4, pp. 713–720, Jul. 1988, doi: 10.1029/RS023i004p00713.

[42] R. Bürgmann, P. A. Rosen, and E. J. Fielding, "Synthetic aperture radar interferometry to measure Earth's surface topography and its deformation," *Annu. Rev. Earth Planet. Sci.*, vol. 28, no. 1, pp. 169–209, May 2000, doi: 10.1146/annurev.earth.28.1.169.

[43] A. Hooper and H. A. Zebker, "Phase unwrapping in three dimensions with application to InSAR time series," *J. Opt. Soc. Amer. A, Opt. Image Sci.*, vol. 24, no. 9, pp. 2737–2747, 2007, doi: 10.1364/josaa.24.002737.

[44] Z. Wu, T. Wang, Y. Wang, R. Wang, and D. Ge, "Deep-learning-based phase discontinuity prediction for 2-D phase unwrapping of SAR interferograms," *IEEE Trans. Geosci. Remote Sens.*, vol. 60, 2022, Art. no. 5216516, doi: 10.1109/TGRS.2021.3121906.

[45] H. J. Jiang, Y. Y. Pei, and J. Li, "Sentinel-1 Tops interferometry for along-track displacement measurement," *IOP Conf. Ser., Earth Environ. Sci.*, vol. 57, Feb. 2017, Art. no. 012019, doi: 10.1088/1755-1315/57/1/012019.

[46] Y. Roa et al., "First assessment of the interferometric capabilities of SAOCOM-1A: New results over the domuyo volcano, Neuquén Argentina," *J. South Amer. Earth Sci.*, vol. 106, Mar. 2021, Art. no. 102882, doi: 10.1016/j.jsames.2020.102882.

[47] A. Ferretti, A. Fumagalli, F. Novali, C. Prati, F. Rocca, and A. Rucci, "A new algorithm for processing interferometric data-stacks: SqueeSAR," *IEEE Trans. Geosci. Remote Sens.*, vol. 49, no. 9, pp. 3460–3470, Sep. 2011, doi: 10.1109/TGRS.2011.2124465.

[48] G. Fornaro, A. Pauciullo, and F. Serafino, "Deformation monitoring over large areas with multipass differential SAR interferometry: A new approach based on the use of spatial differences," *Int. J. Remote Sens.*, vol. 30, no. 6, pp. 1455–1478, Mar. 2009, doi: 10.1080/01431160802459569.

[49] G. F. Carballo and P. W. Fieguth, "Hierarchical network flow phase unwrapping," *IEEE Trans. Geosci. Remote Sens.*, vol. 40, no. 8, pp. 1695–1708, Aug. 2002, doi: 10.1109/TGRS.2002.800279.

[50] G. Dardyk and I. Yavneh, "A multigrid approach to two-dimensional phase unwrapping," *Numer. Linear Algebra Appl.*, vol. 11, nos. 2–3, pp. 241–259, Mar. 2004, doi: 10.1002/nla.380.

[51] A. Baldi, "Two-dimensional phase unwrapping by quad-tree decomposition," *Appl. Opt.*, vol. 40, no. 8, p. 1187, Mar. 2001, doi: 10.1364/ao.40.001187.

[52] Q. Hu, S. Mao, and X. Li, "Phase unwrapping by synthetic weighted multigrid algorithm for interferometric SAR," *Proc. SPIE*, vol. 3721, pp. 2–10, Aug. 1999, doi: 10.1117/12.357624.

[53] G. Fornaro and E. Sansosti, "A two-dimensional region growing least squares phase unwrapping algorithm for interferometric SAR processing," *IEEE Trans. Geosci. Remote Sens.*, vol. 37, no. 5, pp. 2215–2226, Sep. 1999, doi: 10.1109/36.789618.

[54] J. Chen, H. Chen, Z. Yang, and H. Ren, "Weighted least squares phase unwrapping based on the wavelet transform," *Proc. SPIE*, vol. 6279, pp. 1761–1767, Jan. 2007, doi: 10.1117/12.725761.

[55] M. Usui, H. Niki, and T. Kohno, "Adaptive Gauss–Seidel method for linear systems," *Int. J. Comput. Math.*, vol. 51, nos. 1–2, pp. 119–125, Jan. 1994, doi: 10.1080/00207169408804271.

[56] W. L. Briggs, V. E. Henson, and S. F. McCormick, *A Multigrid Tutorial*, 2nd ed., Philadelphia, PA, USA: Society for Industrial and Applied Mathematics, 2000, doi: 10.1137/1.9780898719505.

[57] K. R. James, "Convergence of matrix iterations subject to diagonal dominance," *SIAM J. Numer. Anal.*, vol. 10, no. 3, pp. 478–484, Jun. 1973, doi: 10.1137/0710042.

[58] J. K. Reid, "A method for finding the optimum successive over-relaxation parameter," *Comput. J.*, vol. 9, no. 2, pp. 200–204, Aug. 1966, doi: 10.1093/comjnl/9.2.200.

[59] H. Li, Y. Deng, J. Wang, F. Zhao, Y. Wu, and M. Zheng, "Refined two-stage programming approach to multibaseline phase unwrapping via gradient regularization and quality-guided triangulation," *IEEE Geosci. Remote Sens. Lett.*, vol. 21, pp. 1–5, 2024, Art. no. 4006305, doi: 10.1109/lgrs.2024.3374552.

[60] R. Li, X. Lv, J. Yuan, and J. Yao, "A triangle-oriented spatial–temporal phase unwrapping algorithm based on irrotational constraints for time-series InSAR," *IEEE Trans. Geosci. Remote Sens.*, vol. 57, no. 12, pp. 10263–10275, Dec. 2019, doi: 10.1109/TGRS.2019.2933024.

[61] C. Esch, J. Köhler, K. Gutjahr, and W.-D. Schuh, "One-step three-dimensional phase unwrapping approach based on small baseline subset interferograms," *Remote Sens.*, vol. 12, no. 9, p. 1473, May 2020, doi: 10.3390/rs12091473.

[62] R. K. Ahuja, T. L. Magnanti, and J. B. Orlin, *Network Flows: Theory, Algorithms, and Applications*. Upper Saddle River, NJ, USA: Prentice-Hall, 1993.

[63] D. P. Bertsekas and P. Tseng, "Relaxation methods for minimum cost ordinary and generalized network flow problems," *Oper. Res.*, vol. 36, no. 1, pp. 93–114, Feb. 1988, doi: 10.1287/opre.36.1.93.

[64] Z. Király and P. Kovács, "Efficient implementations of minimum-cost flow algorithms," 2012, *arXiv:1207.6381*.

[65] D. P. Bertsekas and P. Tseng, "Relaxation methods for minimum cost ordinary and generalized network flow problems," *Oper. Res.*, vol. 36, no. 1, pp. 93–114, Jan./Feb. 1988.

[66] K. V. Mardia and P. E. Jupp, *Directional Statistics* (Wiley Series in Probability and Statistics), 1st ed., Hoboken, NJ, USA: Wiley, 1999, doi: 10.1002/9780470316979.

[67] F. Falabella, C. Serio, G. Masiello, Q. Zhao, and A. Pepe, "A multi-grid InSAR technique for joint analyses at single-look and multi-look scales," *IEEE Geosci. Remote Sens. Lett.*, vol. 19, pp. 1–5, 2022, doi: 10.1109/LGRS.2021.3086271.

[68] R. A. Finkel and J. L. Bentley, "Quad trees a data structure for retrieval on composite keys," *Acta Inf.*, vol. 4, no. 1, pp. 1–9, 1974, doi: 10.1007/BF00288933.

[69] H. Samet, "The quadtree and related hierarchical data structures," *ACM Comput. Surv.*, vol. 16, no. 2, pp. 187–260, Jun. 1984, doi: 10.1145/356924.356930.

[70] R. C. Hardie, M. I. Younus, and J. Blackshire, "Robust phase-unwrapping algorithm with a spatial binary-tree image decomposition," *Appl. Opt.*, vol. 37, no. 20, pp. 4468–4476, Jul. 1998, doi: 10.1364/ao.37.004468.

[71] H.-Y. Chen, S.-H. Hsu, W.-J. Hwang, and C.-J. Cheng, "An efficient FPGA-based parallel phase unwrapping hardware architecture," *IEEE Trans. Comput. Imag.*, vol. 3, no. 4, pp. 996–1007, Dec. 2017, doi: 10.1109/TCI.2017.2663767.

[72] C. A. Lee, S. D. Gasster, A. Plaza, C.-I. Chang, and B. Huang, "Recent developments in high performance computing for remote sensing: A review," *IEEE J. Sel. Topics Appl. Earth Observ. Remote Sens.*, vol. 4, no. 3, pp. 508–527, Sep. 2011, doi: 10.1109/JSTARS.2011.2162643.

[73] E. Tymofyeyeva and Y. Fialko, "Mitigation of atmospheric phase delays in InSAR data, with application to the eastern California shear zone," *J. Geophys. Res., Solid Earth*, vol. 120, no. 8, pp. 5952–5963, Aug. 2015, doi: 10.1002/2015jb011886.

[74] F. Falabella and A. Pepe, "On the phase nonclosure of multilook SAR interferogram triplets," *IEEE Trans. Geosci. Remote Sens.*, vol. 60, 2022, Art. no. 5120117, doi: 10.1109/TGRS.2022.3216083.

[75] M. M. Miller, C. E. Jones, S. S. Sangha, and D. P. Bekaert, "Rapid drought-induced land subsidence and its impact on the California aqueduct," *Remote Sens. Environ.*, vol. 251, Dec. 2020, Art. no. 112063, doi: 10.1016/j.rse.2020.112063.

[76] P. Milillo, G. Sacco, D. Di Martire, and H. Hua, "Neural network pattern recognition experiments toward a fully automatic detection of anomalies in InSAR time series of surface deformation," *Frontiers Earth Sci.*, vol. 9, Feb. 2022, Art. no. 728643, doi: 10.3389/feart.2021.728643.

[77] S. M. Mirmazloumi, Y. Wassie, L. Nava, M. Cuevas-González, M. Crosetto, and O. Monserrat, "InSAR time series and LSTM model to support early warning detection tools of ground instabilities: Mining site case studies," *Bull. Eng. Geol. Environ.*, vol. 82, no. 10, p. 374, Oct. 2023, doi: 10.1007/s10064-023-03388-w.

[78] E. Bravo-López, T. F. Del Castillo, C. Sellers, and J. Delgado-García, "Landslide susceptibility mapping of landslides with artificial neural networks: Multi-approach analysis of backpropagation algorithm applying the neuralnet package in Cuenca, Ecuador," *Remote Sens.*, vol. 14, no. 14, p. 3495, Jul. 2022, doi: 10.3390/rs14143495.

[79] S. Schmidl, P. Wenig, and T. Papenbrock, "Anomaly detection in time series: A comprehensive evaluation," *Proc. VLDB Endowment*, vol. 15, no. 9, pp. 1779–1797, May 2022, doi: 10.14778/3538598.3538602.

[80] M. Munir, S. A. Siddiqui, A. Dengel, and S. Ahmed, "DeepAnT: A deep learning approach for unsupervised anomaly detection in time series," *IEEE Access*, vol. 7, pp. 1991–2005, 2019, doi: 10.1109/ACCESS.2018.2886457.

[81] M. Mastyło, "Bilinear interpolation theorems and applications," *J. Funct. Anal.*, vol. 265, no. 2, pp. 185–207, Jul. 2013, doi: 10.1016/j.jfa.2013.05.001.

[82] F. Aurenhammer and Y. Xu, "Optimal triangulations," in *Encyclopedia of Optimization*, C. A. Floudas and P. M. Pardalos, Eds., Boston, MA, USA: Springer, 2001, pp. 1830–1836, doi: 10.1007/0-306-48332-7.

[83] W. Mulzer and G. Rote, "Minimum-weight triangulation is NP-hard," *J. ACM*, vol. 55, no. 2, pp. 1–29, May 2008, doi: 10.1145/1346330.1346336.

[84] A. Lingas, "A new heuristic for minimum weight triangulation," *SIAM J. Algebr. Discrete Methods*, vol. 8, no. 4, pp. 646–658, Oct. 1987, doi: 10.1137/0608053.

[85] L. S. Heath and S. V. Pemmaraju, "New results for the minimum weight triangulation problem," *Algorithmica*, vol. 12, no. 6, pp. 533–552, Dec. 1994, doi: 10.1007/bf01188718.

[86] M. I. Shamos and D. Hoey, "Closest-point problems," in *Proc. 16th Annu. Symp. Found. Comput. Sci. (SFCS)*, Oct. 1975, pp. 151–162, doi: 10.1109/SFCS.1975.8.

Pietro Mastro received the M.S. degree (Hons.) in computer engineering and information technology and the Ph.D. degree in engineering for innovation and sustainable development from the University of Basilicata, Potenza, Italy, in 2019 and 2023, respectively.

He was a Visiting Scientist with the Jet Propulsion Laboratory (JPL), Caltech, Pasadena, CA, USA, in 2023. His main research interests include remote sensing with active and passive sensors, including the development of InSAR algorithms for the monitoring of surface deformation phenomena induced by subsidence, volcano activities, and earthquakes, with a particular interest in noise filtering problems and the application of machine learning algorithms.

Dr. Mastro was a recipient of the Central-North Italy Chapter Best M.S. Degree Thesis in Geoscience and Remote Sensing Award from the IEEE Geoscience and Remote Sensing Society in 2019.

Antonio Pepe (Senior Member, IEEE) received the Laurea degree in electronic engineering and the Ph.D. degree in electronic and telecommunication engineering from the University of Naples Federico II, Naples, Italy, in 2000 and 2007, respectively.

After graduation, he joined the Istituto per il Rilevamento Elettromagnetico dell'Ambiente (IREA), Italian National Research Council (CNR), Naples, where he currently holds a permanent position as a Research Director. He was a Visiting Scientist with The University of Texas at Austin, Austin, TX, USA, in 2005, the Jet Propulsion Laboratory (JPL), Caltech, Pasadena, CA, USA, in 2009 and 2019, and East China Normal University (ECNU), Shanghai, China, from 2014 to 2019. From 2012 to 2017, he was an Adjunct Professor of signal theory at the University of Basilicata, Potenza, Italy. In 2018 and 2020, he was an Adjunct Professor of wireless telecommunication systems at the University of Naples Federico II. He has co-authored more than 90 articles in peer-reviewed international journals. His main research interests include the development of InSAR algorithms for monitoring ground deformation phenomena induced by subsidence, volcano activities, and earthquakes, with a particular interest in phase unwrapping problems. More recently, he has developed research activities for integrating SAR and optical images to analyze land changes in flooded/fired zones.

Dr. Pepe received the 2014 Best Reviewer Mention of IEEE GEOSCIENCE AND REMOTE SENSING LETTERS.

Cathleen E. Jones (Member, IEEE) received the B.S. degree in physics from Texas A&M University, College Station, TX, USA, in 1982, and the Ph.D. degree in physics from the California Institute of Technology, Pasadena, CA, USA, in 1991.

She is a Radar Scientist at NASA's Jet Propulsion Laboratory, California Institute of Technology, where her research is focused on using radar remote sensing to study natural and man-made hazards. Her research interests include the development of methods for identifying hazards affecting flood control and water conveyance infrastructure, and for tracking and characterizing oil slicks to help in response, remediation, and mitigation. She has been the Lead of applications for the NISAR Science Team since 2015.

Open Access funding provided by 'Consiglio Nazionale delle Ricerche-CARI-CARE-ITALY' within the CRUI CARE Agreement